FlySPEX
Channeled Spectropolarimeter for Atmosphere Remote Sensing

Giovanni Paolini

Technische Universiteit Delft

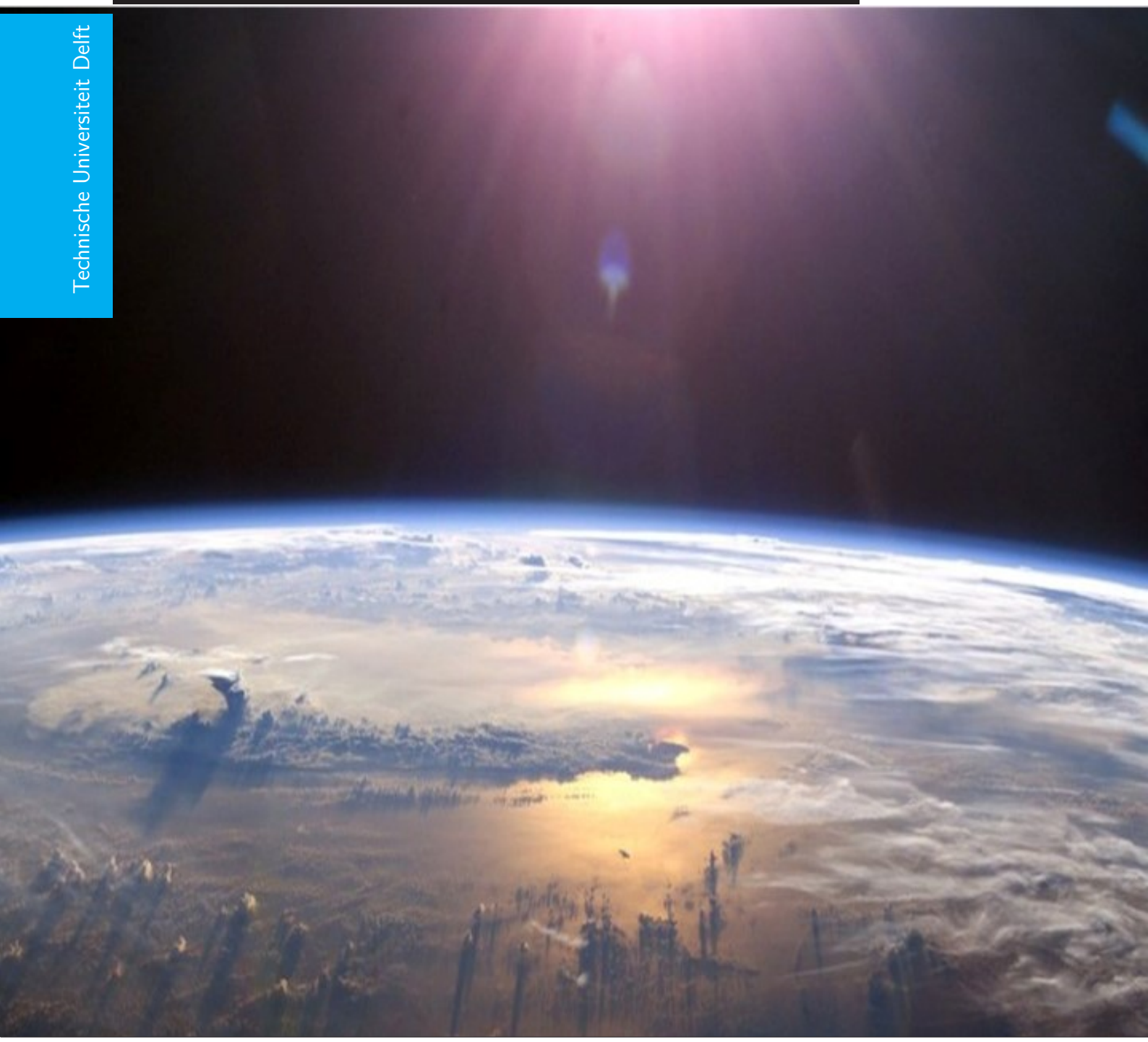

TU Delft Delft University of Technology

Challenge the future

FLYSPEX

CHANNELED SPECTROPOLARIMETRY FOR ATMOSPHERE REMOTE SENSING

by

GIOVANNI PAOLINI
4519167

MASTER OF SCIENCE THESIS
in MSc Aerospace Engineering
Track Spaceflight
Profile Space Exploration

at Delft University of Technology
in collaboration with the University of Leiden

to be defended publicly on September 22nd, 2017

Supervisors: **Dr. Frans Snik** Leiden University / Astronomical Instrumentation
Dr. Daphne Stam TU Delft / Astrodynamics & Space Missions

TU Delft Delft University of Technology

Cover image credits: NASA.gov

ACKNOWLEDGEMENTS

This work would not have been possible without the help and supervision of Dr. Stam, that first introduced me to the topic of polarimetry, giving me the opportunity to discover for the first time the world of astronomy. I also have to thank her for listening to my ideas and objectives, and helping me to find the most suitable thesis topic for me. She shared her knowledge with me and guided me through the last year of this master program. She is also responsible for getting me in touch with the second person I have to thank, Dr. Snik.

Dr. Snik was my daily supervisor, patiently reviewing my progress and listening and evaluating my suggestions and results. I am grateful for his contagious enthusiasm on this topic and for supporting and valuing this work with his expertise. From the first day he encouraged a full hands-on approach, showing me the lab and challenging me to independently set up the experiments.

During my research I also received various suggestions and opinions, that helped me better shape my thesis and its objectives. I have to thank V. Pallichadath from TU Delft, Prof. Keller from Leiden Observatory and the scientists at SRON, J. Ritjens and M. Smit.

My special thanks goes to my family, my mum, Anna, Sara and Giulia, that supported every single academic choice I made during these university years and believed in my dreams before I even did. Another big thanks goes for my friends, the ones in Delft that lived with me those amazing two years, and the ones in Italy that supported me from the distance and never missed a chance to encourage this choice. One last thanks to Ainhoa, my new anchor, the person I am more grateful for the success of this work and these two years.

ABSTRACT

Context. Spectropolarimetry is proposed as a relatively new option in the field of remote sensing for the characterization of aerosol particles and the investigation of cloud properties, that are key factors for the enhancement of climate model's accuracy. The use of multi-wavelength, multi-angle information of the scattered flux and polarization light can lead to the characterization of these particles with unprecedented detail.
Aims. In this context, FlySpex is a new concept of miniaturized spectropolarimeter that features an innovative system for the polarimetric information encoding in a very limited volume. The aim of this work is to assess an initial estimation of this instrument's accuracy, to create a pipeline for the data reduction of the signal received and to perform a feasibility study in order to adapt this technology to a small satellite mission.
Method & Results. In order to assess the performance of the instrument a calibration procedure in the optical laboratory has been performed, using 100% linearly polarized light. A first estimation of the instrument accuracy showed a maximum residual of 0.0056 and a mean residual value of 0.002. A system engineering approach has been developed in order to perform a first study on a space mission concept for the instrument, studying different configurations and analyzing the instrument performance with respect to size, power, pointing accuracy, data rate and resolution of the retrieved data. A 3U CubeSat standard was proposed for the concept of a future space mission and the instrument was adapted to this standard. Twenty viewing points will observe Earth's atmosphere and transmit the signals to a single spectrometer, designed in order to be perfectly compliant with the spacecraft dimensions. Only 1U of the spacecraft is occupied by the payload.

CONTENTS

List of Figures

List of Tables

List of Symbols and Abbreviations

Acronyms

MOR	Multiple Order Retarder
AoLP	Angle of linear polarization
CCD	Charged Coupled Detector
CGS	Compact Grating Spectrometer
CMOS	Complementary Metal-Oxide Semiconductor
COTS	Commercial-Off-the-Shelf
DoLP	Degree of linear polarization of light
DoP	Degree of polarization of light
FOV	Field Of View
GNC	Guidance, Navigation and Control
HWP	Half Wave Plate
IPCC	International Panel on Climate Change
LCP	Left Circular polarized
LEO	Low Earth Orbit
LSQ	Linear Least Square
NA	Numerical Aperture
PCOS	Photonics Crystal Outcoupling Spectrometer
PEM	Photo-Elastic Modulator
PM	Particulate Matter
QWP	Quarter Wave Plate
RCP	Right Circular polarized
SNR	Signal to Noise Ratio
SSO	Sun Synchronous Orbit
SW	Swath Width
TBD	To Be Determined
TRL	Technology Readiness Level
TU	Technische Universiteit

Variables

α	inclination angles incident beam on the grating
β	inclination angles reflected beam on the grating
χ	Polarization angle or azimuth of the polarization
Δ	Retardance
ϵ	Polarimetric efficiency vector
A	Angular dispersion
a	Electric field amplitude
D	Diameter
d	line spacing length on the grating
F#	F number
f	Focal length
H	Altitude
I	Intensity vector
m	grating order
$\mathbf{N_{el}^{o}}$	Number of detector resolution elements
n	Refractive index
$\mathbf{P_L}$	Degree of linear polarization of light
r	resolution
$\mathbf{T_p}$	Extinction Ratio parallel linear polarization
$\mathbf{T_s}$	Extinction Ratio perpendicular linear polarization
$\mathbf{tan}(\beta)$	Axial ratio of the ellipse
t	transmission ratio of the two channels of FlySPEX
$\mathbf{W_{pix}}$	Total number of pixel used for one spectra
w	Slit width
w	width for one resolution element
D	Demodulation Matrix
O	Modulation Matrix
X	Polarimeter Response Matrix
M	Mueller Matrix
Q	Linear polarized Flux expressed as a Stokes parameter $(0, \pm 90^o)$
R	Spectrograph Resolving Power
S	Normalized difference between the two channels
U	Linear polarized Flux expressed as a Stokes parameter $(\pm 45^o)$
V	Circular polarized Flux expressed as a Stokes parameter

1

INTRODUCTION

1.1. GENERAL BACKGROUND

The aim of this thesis project is to provide an initial study on a new concept of optical instrument in the field of Spectropolarimetry, FlySPEX. This instrument has been developed by the university of Leiden [3] and it will address mainly the demand from the scientific community of accurate retrieval of the properties of aerosol particles.

The official call for an intensive investigation on aerosol particles concentrations and their properties was produced after the IPCC (Intergovernmental Panel on Climate Change) conference in 2003 [4]. In the document aforementioned, a discussion about the influence of aerosol particles properties on atmospheric and radiative model has been addressed, concluding that it is nowadays the cause of the greatest uncertainties on climate change prediction. Moreover, the impact of so-called fine dust, which are very small aerosol particles, on human health revealed respiratory problems in the long term, such as reduced lung function in asthmatic children [5] and increased lung-cancer mortality in adults [6][7], as well as in the short term, such as an increase in cardiopulmonary hospital admission and mortality [8][9].

In order to address this problem, a number of instruments have been developed to provide information on aerosol's composition and distribution, either ground-based or space-based. Ground-based instruments as Particulate Matter (PM) monitoring and Sunphotometer do not provide a sufficient spatial coverage, they also provide limited information, delivering only the particles' size and a rough characterization of aerosols through the imaginary part of the refractive index. Various space missions involved in aerosol properties retrieval exist: PARASOL/POLDER in the past, MODIS and MISR currently operational, and in the future the instruments MISR, APS and PACS [10]. Some of these operational space instruments can deliver multi-angle, multi-wavelength information, allowing the particles' size and refractive index retrieval. Nonetheless, only the PARASOL/POLDER mission featured polarimetric information, necessary for improving micro and macro properties of aerosol particles and for aerosol particles detection near and above clouds. This is a crucial information, since aerosols are suspected to act as cloud condensation nuclei. Moreover, current instruments do not deliver accurate enough data, useful to understand the aerosol radiative forcing down to the 0.25 W/m^2 level, as required in [11]. This level is only reachable with a polarimetric accuracy of around one level of magnitude better than the operational one [12].

The new generation of instruments, together with the SPEX family which FlySPEX belongs to, will be able to reach that level of accuracy [10].

FlySPEX will deliver multi-angle, multi-wavelength spectropolarimetric information, addressing all the requirement for a fully characterization of aerosol particles only occupying a fraction of the volume needed for the previous spectropolarimeters and with a lightweight structure. These characteristics are essential for a space mission and will lead to a drastic cut in the classic cost budget for a scientific mission. Its adaptability to a cubeSat standard is also an essential element, since it further cuts the mission costs with the use of off-the-shelf components and it is directly suited for a future multi-satellite mission (since research is towards swarms, formation flying or constellation satellite systems). Since the design of the instrument is very flexible, it can also address different objectives, such as studies on a major component in air pollution, NO_2, whose data are currently insufficient [3].
Other applications listed in [3] for the FlySpex concept are its use as nephelometer and particle counter and, not linked with space missions, are bio-medical diagnostic imaging, food quality control and generic laboratory fiber polarimeter.

The peculiarity of the FlySPEX instrument relies on its fiber-head nature, which means that all the optics (of the polarimeter) are miniaturized at the top of two optical fibers that transmit the information taken from a single viewing point to the second part of the instrument (the spectrometer).
The shape of the first prototype is shown in Figure 1.1. The innovation led by the instrument also lies in its snapshot nature: with just one observation all the aerosol properties of a precise region are imaged, allowing to virtually eliminate all the differential effects and errors, typically present in other polarimeter instrument designs.
Important elements needed for the data reduction process are retrieved from the calibration, and a first insight on the instrument performance can be inferred.

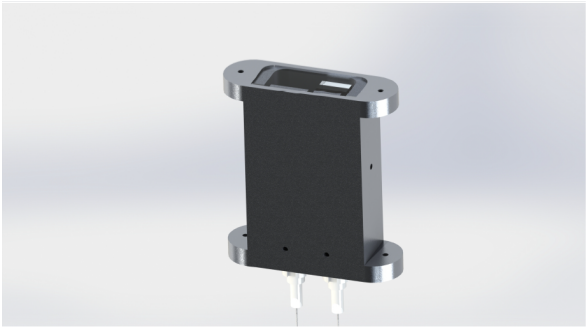

Figure 1.1: Figure from [3]. Rendering of the mechanical design of FlySPEX fiber head. The unit contains the polarization optics that split the light in two beams, the light then goes to the spectrometer (not shown in the picture) through the two fibres. The prototype dimensions of the fiber-heads are currently $32x29x10\ mm^3$.

This thesis is divided in two parts, since two needs are addressed: the in-lab calibration of the instrument prototype, in order to assess the accuracy level of the instrument, and a first concept design, in order to enable the integration of the instrument in a future small satellite mission observing the Earth. In the first part of the thesis, results from a first calibration of the spectropolarimeter are presented.

The second part of this thesis will be focused on the concept design of an instrument for a future Earth remote sensing mission, that will study the lower part of the atmosphere providing multi-angle multi-spectral capability. In the following sections of this introduction, the technique behind the channeled instruments and the optical elements characterizing this family of instruments will be better explained, beginning with some common notions on polarimetry.

1.2. THEORETICAL BACKGROUND - POLARIMETRY

Polarization is a fundamental property of light that describes the geometrical orientation of the oscillation of the electromagnetic wave. Given the orthogonality of the electric and magnetic field, traditionally only the former one is used as a reference to describes the geometrical position in space of the wave.

Generally speaking, polarization indicates anisotropy, a preference on the orientation on the wave oscillation's direction, thus a break of the symmetry. Polarization can be either inherent to the source of light, or created by the medium between the detector and the source, or both. One fundamental concept, important to stress, is that polarimetric information is essential to give a complete description of the content of light radiation. Classical detection of light as a scalar quantity is not able to describe its polarimetric content, thus a vectorial form is required. The polarization state, dependent on position, wavelength and time, gives the possibility to remotely obtain information on a wide range of sources and objects.

1.2.1. KEY POLARIMETRIC ELEMENTS

STOKES PARAMETERS

Stokes parameters represent a method of describing intensity and geometrical orientation of light through the use of four elements: these four parameters define the so-called flux vector. This formalism was introduced by Sir George Gabriel Stokes [13] and adopted in astronomy by Chandrasekhar in his monumental dissertation on radiative phenomena [14].

As stated in [15] and reviewed in [16], while there is a mathematical convention on the formalism, there is no similar thing on the denotation of the Stokes parameters. In order to be consistent during this dissertation, the notation illustrated below, which is also adopted by the majority of the astronomical/atmospheric community, will be used.

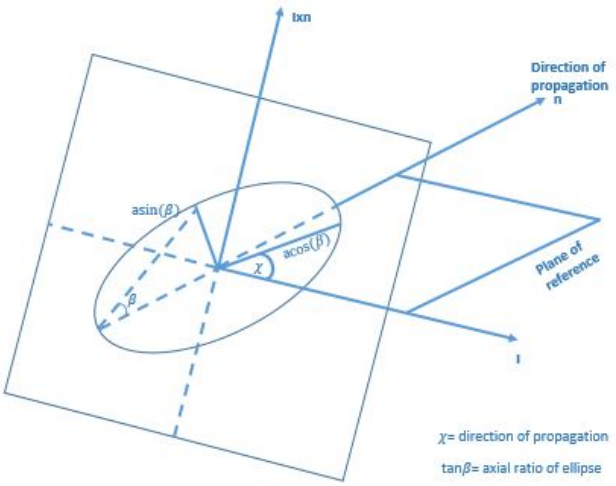

Figure 1.2: Adapted figure from [15], Presentation and Visualization of the Stokes parameters in a right-handed elliptical fashion where V is positive. The unit vectors I, n and Ixn constitute the reference frame.

Figure (1.2) presents the Stokes parameters and Equation (1.1) shows the definition of the Stokes parameters based on that convention.

$$\begin{pmatrix} I \\ Q \\ U \\ V \end{pmatrix} = \begin{pmatrix} a^2 \\ a^2 cos2\beta cos2\chi \\ a^2 cos2\beta sin2\chi \\ a^2 sin2\beta \end{pmatrix} \tag{1.1}$$

In general, a "polarization ellipse", as defined by Tinbergen, is used to characterize the signal: this ellipse describes the movement of the tip of the electrical field vector, as it changes with time. The flux vector summarizes the content of the ellipse. It is respectively formed by the intensity vector I, which is simply the square of the intensity of the electrical field a, the parameters Q and U, that represent a linear oscillation of the electric field in the two perpendicular planes, and finally the vector V, that represents the circular oscillation of the tip of the electrical field vector. The ellipse is then the general case, nothing else than the combination of linear and circular oscillation. The two angles χ and β are defined in the figure.

A more practical and instrument-oriented definition of the Stokes parameters has been formulated in [17]. This definition is useful to introduce the theory of instrument modelling through the Mueller formalism, that will be illustrated later in this chapter and extensively used for the instrument model.

$$\begin{pmatrix} I \\ Q \\ U \\ V \end{pmatrix} = \begin{pmatrix} I'_{0^o} + I'_{90^o} \; or \; I'_{-45^o} + I'_{45^o} \; or \; I'_{LHC} + I'_{RHC} \\ I'_{0^o} - I'_{90^o} \\ I'_{45^o} + I'_{-45^o} \\ I'_{RHC} + I'_{LHC} \end{pmatrix} \tag{1.2}$$

This definition is formulated using the photon flux I', and gives a more operational view, since the quantities (I'_Ψ) are the equivalent of flux measurement on the detector, obtained through a polarizer inclined at different angles Ψ, as indicated in Figure 1.3b (RHC and LHC indicate right and left handed circular polarization). From the instrument point of view, the

angle Ψ is the orientation of the polarizer measured anticlockwise with respect to the direction perpendicular to the optical table. The angle Ψ can assume another definition when using a different reference frame: from the observed object's point of view, the orientation of the angles described in eq. (1.2) is based on the deviation of the electric field vector from the commonly adopted scattering plane, described in papers as Hansen & Travis, 1974 [18]. The paper defines the scattering plane as the plane that contains the direction of incidence and scattering of the wavelength. The angle indicated in eq. (1.2) and called Ψ in Figure (1.3b) is then measured anticlockwise from the scattering plane.

To convert the Stokes vector from the measured scattering plane to the optical plane of the polarimeter the so-called rotation matrix L can be used [19] [2]:

$$\mathbf{L} = \begin{bmatrix} 1 & 0 & 0 & 0 \\ 0 & cos(2\beta) & sin(2\beta) & 0 \\ 0 & -sin(2\beta) & cos(2\beta) & 0 \\ 0 & 0 & 0 & 1 \end{bmatrix} \tag{1.3}$$

This matrix operator apply a change in reference system rotating anticlockwise from old to new reference plane through the use of the angle β.

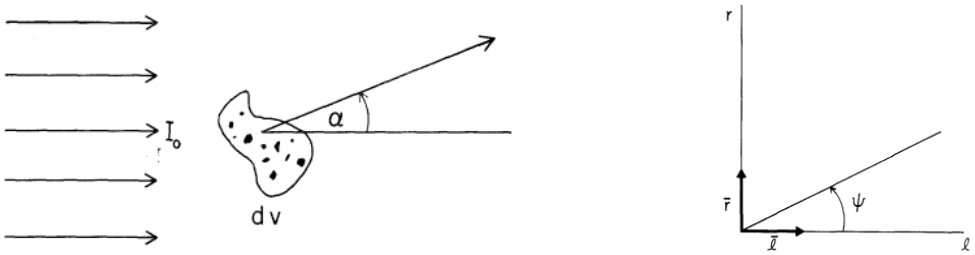

(a) **(b)**

Figure 1.3: Figures from [18]. a) Visualization of the scattering angle. b) description of the polarization angle Ψ with respect to the propagation direction $\bar{l}$ and the normal to the scattering plane $\bar{r}$.

Looking again at eq. (1.2), it is clear why polarimetry is defined as a differential technique: considering that the instrument can measure only intensities at different polarization angles, then it is clear that at least two intensities need to be retrieved in order to produce one polarized Stokes parameter Q, U or V.
The Stokes parameters are usually normalized by the intensity I, in order to eliminate the dependency of these parameters on the intensity of the signal detected. When normalized by the intensity, the notation changes to lower case: q, u, v.
Other commonly used parameters are the degree of polarization:

$$DoP = \frac{\sqrt{Q^2 + U^2 + V^2}}{I} \tag{1.4}$$

The degree of linear polarization (particularly useful when circular polarization is negligible):

$$DoLP = \frac{\sqrt{Q^2 + U^2}}{I} \tag{1.5}$$

And the angle of linear polarization:

$$AoLP = \frac{1}{2} atan2\left(\frac{U}{Q}\right) \tag{1.6}$$

The term "atan2" refers to the arctangent function, but it is a slightly modified version that takes into account the sign of the two divided elements, in order to avoid any ambiguity in the retrieved angles (the codomain of this function becomes $[0, 2\pi]$) [18]. with the use of this function, AoLP values can be retrieved from 0 to π.

MUELLER MATRIX

Another useful mathematical tool derived from the Stokes formalism is the Mueller matrix, a $4x4$ matrix that ideally describes every interaction of the wave with matter, in a linear fashion.The incoming light, described by the vector S_{in} (the previously mentioned flux vector), will be changed and manipulated by the medium and the optics, resulting in the received S_{out}, so that:

$$\mathbf{S_{out}} = \mathbf{M} \cdot \mathbf{S_{in}} \tag{1.7}$$

Where the Mueller matrix is:

$$\mathrm{M} = \begin{bmatrix} I \to I & Q \to I & U \to I & V \to I \\ I \to Q & Q \to Q & U \to Q & V \to Q \\ I \to U & Q \to U & U \to U & V \to U \\ I \to V & Q \to V & U \to V & V \to V \end{bmatrix} \tag{1.8}$$

POINCARÉ SPHERE

A refined and immediate way of describing the effects of any medium on the incoming light, is to represent them graphically, on the Poincaré sphere. This sphere is the equivalent of the Mueller matrix, that describes polarization changes as the movement of a vector in a $3D$ coordinate system, formed by the normalized parameters q, u, v. This vector will be always fully contained in a sphere with radius 1.

The centre of the sphere describes fully unpolarized light, while the surface contains fully polarized light ($DoP = \sqrt{q^2 + u^2 + v^2} = 1$) or, if it lays on the equator, the vector is just linearly fully polarized with $DoLP = \sqrt{q^2 + u^2} = 1$. Any other combination results in a partial polarization, represented by any place inside the sphere.

As it will be presented in the section regarding the instruments set-up, any element that composes a polarimeter can be described by a Mueller matrix, and a movement on the Poincaré sphere.

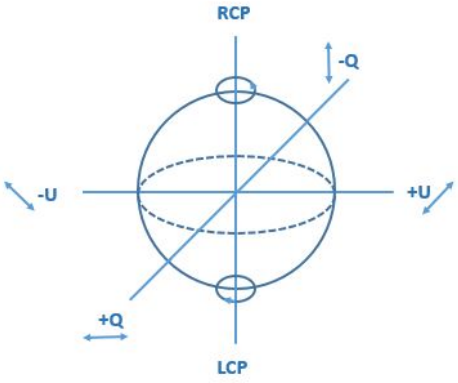

Figure 1.4: Figure from [20], representation of the Poincaré sphere. RCP (right circular polarization) is considered the positive parameter v, LCP (left circular polarization) is $-v$.

1.2.2. POLARIMETRIC ACCURACY, SENSITIVITY AND EFFICIENCY

SENSITIVITY

Polarimetric sensitivity is defined as the lowest polarization level of the source that is still discernible from spurious polarization signals due to noise.
It is generally expressed as a percentage of the intensity I.

ACCURACY

Accuracy defines how close to the input Stokes parameters the instruments can read the signal. It is then a key parameter to describe the instrument requirements and it is strongly dependent on the calibration process and the data reduction. This can be mathematically translated by the matrix X (in [17]):

$$\mathbf{S_{out}} = \mathbf{X} \cdot \mathbf{S_{in}} \tag{1.9}$$

where X is a $4x4$ matrix ("polarimeter response matrix" as firstly introduced in [21]) and can be decomposed in $\mathbf{X} = \mathbf{I} + \Delta\mathbf{X}$, being $\mathbf{I}$ the identity matrix and $\Delta\mathbf{X}$ the accuracy matrix that describes the uncertainties and cross-talk between the four parameters.
The matrix shows many similarities with the Mueller matrix, but it is not identical, since it also includes the effects of data reduction and calibration. The goal of a complete calibration process is reaching the highest accuracy possible [22].

EFFICIENCY

The last important quantity for the assessment of a polarimeter is the polarimetric efficiency. This quantity is strongly related with the quality and quantity of observations and the instrument calibration process. It generally described the performance of the given polarimeter with respect to statistical noise.
Efficiency is a f1our vector quantity derived from the demodulation matrix $\mathbf{D}$, that is defined from the following relation:

$$\mathbf{S_{out}} = \mathbf{D} \cdot \mathbf{I}' \tag{1.10}$$

where $\mathbf{S_{out}}$ are the elaborated stokes parameters from n observations that lead to the photon flux noise $\mathbf{I}'$. The demodulation matrix will be better described in section (1.2.4) since it is

highly involved in the calibration process. From the demodulation matrix, the four-element vector ϵ, indicating the system efficiency, is described as:

$$\epsilon_k = \left(n \sum_{l=1}^{n} D_{kl}^2 \right)^{-\frac{1}{2}} \tag{1.11}$$

1.2.3. POLARIMETER OPTICAL ELEMENTS

The FlySpex instrument is composed by elements that are at the base of every polarimeter, thus a review of the basic optical elements is here presented, in order to illustrate the instrument set-up and mathematical model.

POLARIZER

Polarizers can be defined as "filter for polarization states" [17]. Their main aim is to divide the different polarization states, either by transmitting only one polarization state (linear polarizer) or both polarization states of light at perpendicular linear polarization directions (Beam-splitter Polarizer).

The most used linear polarizers are Polaroid film (aligned anisotropic crystals or polymers) and wire grid (aligned conductive wires). For Polaroids the non transmitted beam is absorbed, while it is often reflected in wire grids.

Beam-splitters are more efficient mechanisms, since they transmit all the received photon flux. Most of them are based on birefringent crystals, that have two different refractive indices for the perpendicular ordinary and extraordinary wave, n_o and n_e, respectively, thus two different refractive angles, according to Snell law.

An ideal polarizer, transmitting in the axis $\pm Q$, is represented by the following Mueller matrix:

$$\mathbf{M_{pol}} = \begin{bmatrix} 1 & \pm 1 & 0 & 0 \\ \pm 1 & 1 & 0 & 0 \\ 0 & 0 & 0 & 0 \\ 0 & 0 & 0 & 0 \end{bmatrix} \tag{1.12}$$

The respective movement in the Poincaré sphere is a projection of the vector on the $\pm Q$ or, more generally, into the axis of the polarizer. The Mueller matrix for a non-ideal polarimeter will be shown in chapter 4.

RETARDER

Retardance is a property of some materials, that can introduce phase shift between the propagation of the two components of the wave (its electric field) along two orthogonal axis, respectively the fast and slow axes. A retarder is characterized by its axis orientation and its retardance angle Δ. This retardance can be controlled, given its dependence on the thickness of the plate and the ordinary and extraordinary axes refractive indexes, with the following formula:

$$\Delta = \frac{2\pi \cdot d}{\lambda}(n_e - n_o) \tag{1.13}$$

The most common retarders (also called wave-plate) are the ones that induces a phase shift of $\Delta = \pi/2$ and $\Delta = \pi$ and they are respectively called quarter wave plate (HWP) and half wave plate (HWP). The shift created by the QWP changes U into V and vice versa, while the one induced by a HWP exchanges the value of the linear parameter Q into U, mirroring them along the fast axis.

An ideal retarder is represented by the following Mueller matrix:

$$\mathbf{M_{ret}} = \begin{bmatrix} 1 & 0 & 0 & 0 \\ 0 & 1 & 0 & 0 \\ 0 & 0 & cos(\Delta) & sin(\Delta) \\ 0 & 0 & -sin(\Delta) & cos(\Delta) \end{bmatrix} \tag{1.14}$$

Visually, a retarder rotates the vector by an angle Δ with respect to the representation of the fast axis on the Poincaré sphere. The respective movement in the Poincaré sphere is shown on figure below, together with the representation of the effects of the two mostly used wave plate (QWP and HWP).

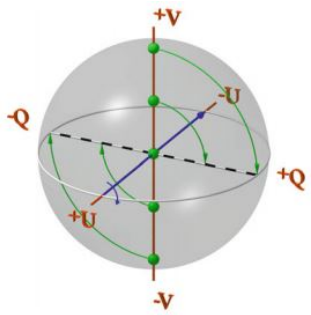

Figure 1.5: Figure from [17], representation on the Poincaré sphere of the effect of a QWR on a polarized signal. Fast axis on the U direction and Polarizer in the $+Q$ direction.

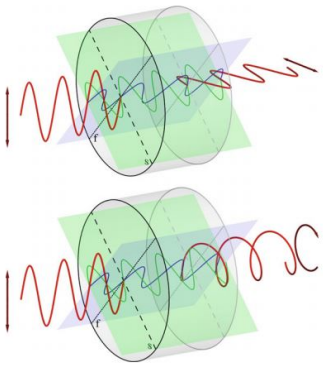

Figure 1.6: Figure from [17], graphic representation of the QWP and HWP effect on the incoming wave. The upper figure shows a HWP that mirrors the wave with respect to the fast axis, and below a QWP that exchanges linear polarization with circular.

1.2.4. MODULATION TECHNIQUES

Even though a polarimeter has a simple set up, which is generally fixed in order and components, strong differences are found in the way the polarimetric information is encoded. Since at least two measurements are needed, different strategies in order to retrieve the polarimetric information has been developed, named as modulation techniques.

Historically, two types of modulations are used for the large part of polarimeters: spatial modulation and temporal modulation [17].

Spatial modulation is described as the splitting in two (or more) beams, containing different polarization states, that arrives at the detector/detectors (for classical photometry) or a spectrograph/spectrometer (for an analysis along the wavelength).

Temporal modulation is performed through a retarder installed before the polarimeter (also called analyzer) that rotates to sequentially obtain different polarization states from the photon fluxes. The orientation of the retarder is fundamental, since different angles give different modulation of the information. Snik & Keller [17] presented the modulation formula, based on the received intensity signal I' after the polarizer in an ideal instrument, with a retarder that introduces a delay Δ and can be rotated by an angle α:

$$\begin{aligned} I'(\Delta,\alpha) = \frac{1}{2}\Big(I + \frac{Q}{2}\left((1+cos\Delta) + (1-cos\Delta)\,cos4\alpha\right) + \\ + \frac{U}{2}(1-cos\Delta)\,sin4\alpha - V sin\Delta\ sin2\alpha\Big) \end{aligned} \tag{1.15}$$

This equation is obtained with the Mueller calculus applied on a rotating retarder and a polarizer. The temporal modulation is shown as dependent on the rotation angle α of the modulator (the retarder wave plate).

These two approaches are ideally similar, thus both result reasonable if we consider an ideal instrument with perfect behaviour. In reality, spurious polarization signals strongly influence the output of the instrument, when taking into account differential effects, and both modulation configurations present strong limitations.

Temporal modulation is limited by change on the observed region for slow modulation, since changing the assets of the instrument between two exposures may require too much time and lead to observing the target when it is drifted, or changed in intensity or polarization (this is often verified for the classic set up with a rotating quarter wave plate, that has also the drawback of being a movable part, thus subjected to higher failure risk).

Solutions have been proposed, in order to avoid this long delay between two exposures: the most important ones are replacing the retarder with liquid crystal (birefringent elements with variable retardance that can be oriented inducing a specifically oriented electric field on the component) or using a Photo-Elastic Modulator (PEM, elements whose orientation and retardance is dependent on the stress level applied on the element). These fast modulations needs a very fast demodulator, thus specific detectors capable of read-out rates with the same or higher modulation frequencies needs to be designed, and that can be a strong limitation. On the other hand, spatial modulation also presents drawbacks responsible for decreasing the ideal sensitivity level introducing spurious signals. These drawbacks

are: transmission differences among the beams, differential aberrations, larger detectors and flat field differences [23].

A good sensitivity result (in the order of 10^{-5}) is obtained with the so-called dual beam technique [24] [15][25]). This technique involves the combination of the two modulations: the system is composed by a wave plate and a beam-splitter, so that it always analyses all the incoming flux and allows for long exposure. Double difference and double ratio are the two data reduction techniques used to eliminate spurious effects and reach that sensitivity level, that will then be only limited by Poisson photon noise, as explained in the papers aforementioned.

Instead of this two classical modulation techniques, an innovative approach is in developing process after [26] and [27] independently reinvented the concept introduced by Nordsieck [28], that proposed a particular set up for polarimeter instruments working in the wavelength domain. This invention exploits the wavelength domain to encode the polarization information, together with the intensity value, so that it becomes possible to instantaneously retrieve all the Stokes parameters with one observation. This is a fundamental advantage, since all the differential effects that affected the sensitivity level are eliminated and the effectiveness of the data reduction process is then the main limit to the performance, together with Poisson noise. Also, accuracy is expected to strongly increase, since it will only be affected by thermal effects and alignment of instrument optics: designing an athermal wave plate helps to reach a really high accuracy level [29].
The approach will be further explained in Section (1.2.5).

1.2.5. CHANNELED SPECTROPOLARIMETER SET UP

SPECTRAL ENCODING TECHNIQUES

Channeled (spectro)polarimetry is a new approach (developed by Oka & Kato [26]), that encodes the polarimeter information in the spectral domain. To obtain these results, a set up with two retarder plates has been used, oriented at 0^o and 45^o with respect to the polarizer main axis. This wave plate features a variable retardance, dependent on the wavelength.

The Oka & Kato instrument then modulates the intensity with the following formula:

$$I'(\lambda,\Delta_1,\Delta_2) = \frac{1}{2}\Big[I_{in}(\lambda) \pm \Big[Q_{in}(\lambda)cos(\Delta_2(\lambda)) + \\ + U_{in}(\lambda)sin(\Delta_1(\lambda))sin(\Delta_2(\lambda)) - V_{in}(\lambda)cos(\Delta_1(\lambda))sin(\Delta_2(\lambda))\Big]\Big] \tag{1.16}$$

This equation differs strongly from the time-modulation equation (1.15), since it shows the wavelength dependence of the two retarders, that allows this spectral encoding.
It is important to stress that this method marks a strong change in the polarimeter set up, since it allows with just one exposure to get all the information contained in the Stokes parameters, no more affected by differential effects. It is also remarkable that this kind of instruments perform observations with no need of movable parts on the modulator, thus, lowering down power consumption and failure possibilities.
On the other side, one drawback of this approach lies in the spectral modulation itself. From a manipulation of eq. (1.16) three different modulation frequencies can be isolated (respectively dependent from Δ_2 and $\Delta_1 \pm \Delta_2$), these modulations are proportional to $\frac{1}{\lambda}$. From

this consideration, it is evident how spectral resolution needs to be large enough to allow a proper encoding, thus the instrument requires a more accurate spectrometer.

Other set-ups have been investigated beginning from this new encoding proposal: one solution [29] in order to solve the issue linked to the high spectral resolution requirement is the design of an instrument only focused on broad band detection of linear polarimetry. This approach relaxes the requirements for the general spectropolarimeter and is optimized for planetary atmosphere study, where circular polarization is often many magnitude orders smaller than the linear polarization, and the polarization of aerosol does not show strong changes in the spectral domain (even though gaseous absorption bands may have strong spectral features).

With this approach, the number of modulation frequencies is reduced to one and the increase in spectral resolution is minimal. The system will modulate the degree and angle of linear polarization (respectively $DoLP$ and $AoLP$). The instrumental set up is generally composed by an achromatic quarter wave-plate (QWP) and an athermal multiple order retarder (with retardance $\Delta(\lambda)$). In this case, the intensity is modulated as:

$$I'(\lambda) = \frac{1}{2} I_{in}(\lambda)\left[1 \pm DoLP(\lambda) cos(\Delta(\lambda) + 2AoLP)\right] \tag{1.17}$$

Or, expressed in terms of Stokes parameters:

$$I'(\lambda) = \frac{1}{2} I_{in}(\lambda)\left[1 \pm q(\lambda) cos(\Delta(\lambda)) + u(\lambda) sin(\Delta(\lambda))\right] \tag{1.18}$$

This is the set-up created for the SPEX instrument and inherited, with some changes, in the FlySPEX concept, explained in more detail in the following section (1.2.5).

SPECTROPOLARIMETER ELEMENTS

FlySPEX is a channeled spectropolarimeter, that encodes the information along the spectral domain [3]. The peculiarity of the instrument is the fiber-head that contains the polarization optics involved in the modulation of the beam. Thanks to this concept instrumental polarization effects are minimized, since the polarization is encoded in the spectral domain and is not subject to any modification from the optics behind the modulator. Since the optics inside the fibers are of millimeter order, no instrumental effect due to mechanical stress and field angle is created, virtually defining the concept as instrumental error-free. The field of view of each fiber head is necessarily small, accepting at normal incidence a 1^o x 1^o beam.

The components of the instrument can be presented, basing the description on [3] and its predecessor, the SPEX instrument [10] [30] [31] [32].
A general scheme of the set-up of the SPEX instrument is shown in Figure (1.7).

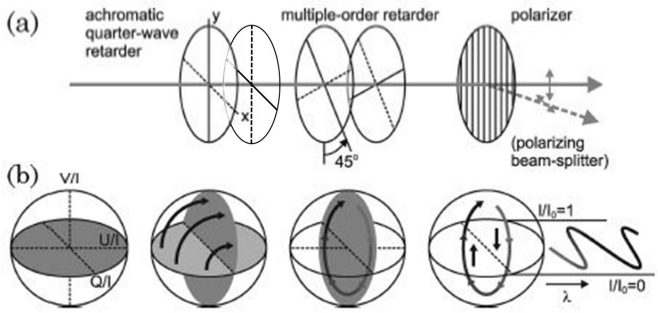

Figure 1.7: Figure from [29] adapted for FlySpex (two plates used as a quarter wave-plate). Set up of the instrument (a) and illustration of the spectral modulation principle on the Poincaré sphere (b).

From the figure, it is possible to see how the beam is modulated: first the quarter wave-plate exchanges the Stokes U in V and vice versa, then the two Multiple order retarders modulate the signal present in the plane $Q-V$ that is spectrally encoded. The polarizing beam splitter then has the effect of projecting the modulation on the Q axis, creating two signals that are 180^o shifted. The image only represents the spectral modulator part of the instrument, that will be followed in FlySpex by two optical fibers connected to a spectrometer.

FlySpex differs from SPEX set-up since instead of the achromatic quarter wave-plate retarder it has two thin plates of quartz and MgF_2 with their fast axes normal to each other to form a 3/4-wave plate: this choice was made due to the compactness of this set up (with respect to the Fresnel romb used for SPEX [3]) and because it can accommodate polishing. The Multiple Order Retarder (MOR) consists as well of two plates of quartz and MgF_2, with the fast axis normal to each other and inclined 45^o and -45^o with respect to the transmitting axis of the first channel of the polarizer, that is a beam splitter. This beam splitter is composed, in the realized prototype, of a rhomboid with a dielectric coating at the hypotenuse to split the beams perpendicularly between each other, and a triangular prism that through internal reflection redirects the second beam to the entrance of the second fiber, to be parallel with the first beam.

An example of the spectral modulation of SPEX is shown in Figure (1.8), where the polarization information is encoded in the spectra on the first part of the image and extrapolated and normalized in the second part (through the difference over the sum of the two beams that will isolate the polarized properties of the wave, as it is possible to notice in the general formula of eq. (1.17)). Similar results will be presented for the calibration outcomes of FlySPEX.

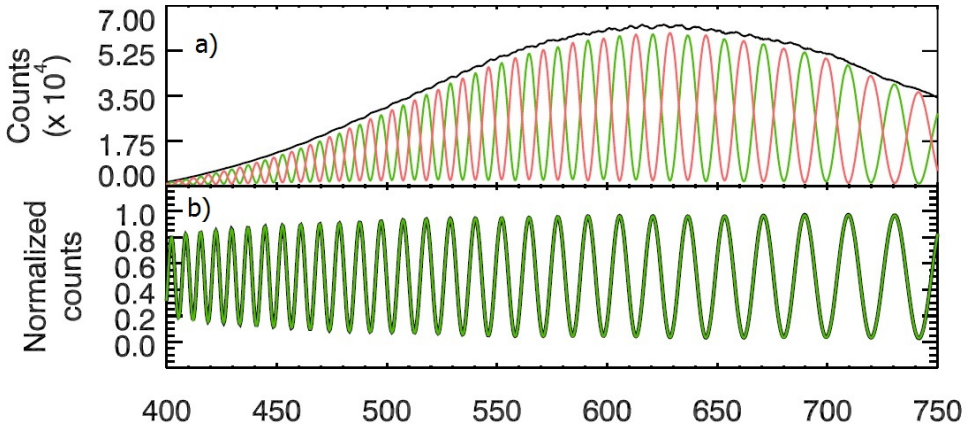

Figure 1.8: Figure from [10], results from one snapshot of SPEX (a, green and red lines), and intensity of the spectra from the sum of the signal. Normalization of the spectrum by the subtraction of the sum of the two signals (b).

Part I:

Simulations & Calibration

2

INTRODUCTION TO PART I

The focus of Part I is the identification of the principal polarimetric errors introduced by the different elements of the FlySPEX instrument. The work has been performed in the optical laboratory of the Astronomical department of Leiden University.
An initial set of raw data is acquired using a 100% polarized light oriented in a set of different angles ranging from $+Q$ to $-Q$.

Before the calibration procedure, corrections for transmission difference of the two channels and for the non perfect extinction ratios of the polarizer beam-splitter are applied. A fitting algorithm is then used to the set of data to obtain the fitting parameters of the curve corresponding to the Angle of Linear Polarization (AoLP), the Degree of Linear Polarization (DoLP) and the MOR retardance $\Delta(\lambda)$.

From these parameters efficiency curves are obtained. The fully polarized light in the $+Q$ direction will produce a DoLP that will be used as efficiency curve $\epsilon_{DoLP}(\lambda)$.

As a second order correction, another calibration curve is extracted from the DoLP intensity variations at different AoLP along all the wavelength. This variation is modelled as periodic of $\pi/2$ due to the non-perfect behaviour of the QWP, that decrease the retrieved polarization along the $+U$ direction, as discussed further in the chapter.

Chapter (3) will explain the optical elements used for this research and the general set-up. Chapter (4) will illustrate the numerical model built to simulate the instrument, used finally to check for consistency of the results. Chapter (5) will explain the calibration procedure used and will show the calibration curves obtained. Finally, Chapter(6) will show the procedure selected for the data retrieval process and the results of the laboratory work.

3

CALIBRATION SET-UP & ELEMENTS USED

The experiments addressed in this section have been performed at the optical laboratory of the Astronomical department of the university of Leiden. In order to perform a polarization calibration of the instrument, a 100% polarized light is used as an input for the instrument, through the use of a halogen lamp to ideally produce an homogeneous unpolarized source. The polarimeter will completely polarize the source.

The elements used were a tungsten halogen source, model HL-2000 from OceanOptics (wavelength range: $360-2400\ nm$), a Glan-Taylor calcite linear polarizer, model GT10 from Thorlabs, with an extinction ratio of $100000:1$ with a rotation mount that will allow to change the angle of linear polarization of the source. A neutral density filter is just an additional element to prevent the saturation of the spectrograph's detector. The spectrograph used for all the experiments is a dual channel fiber optic spectrometer produced by Avantes, with a wavelength range from 200 to 1100 nm, with a 2048 pixels CCD detector and a grating that features 300 lines/mm, $1,3\ nm$ resolution.

The experiment consists of acquiring a data-set of the instrument response for a varying input sources, composed by a 100 % linearly polarized light set at different polarization angles. This angle was varying between 0 and 360 deg. with a step of 10^o. Exposure at $\pm\ 45^o$ and $\pm\ 135^o$ were also taken being the directions of the $\pm\ Q$ polarized light. The angle of linear polarization is periodic of 180^o, thus the data-set taken from 180^o to 360^o are repeated, but still acquired for redundancy.

This experiment was repeated with different campaigns, from February 2017 to June 2017, and a different configuration was also adopted for some of the experiments, replacing the collimated light source with an homogeneous integrating sphere, as shown in Figure (3.2). These configuration was used in order to have a more homogeneous light source an it proved to be more precise, thus it was adopted for the last experiments.

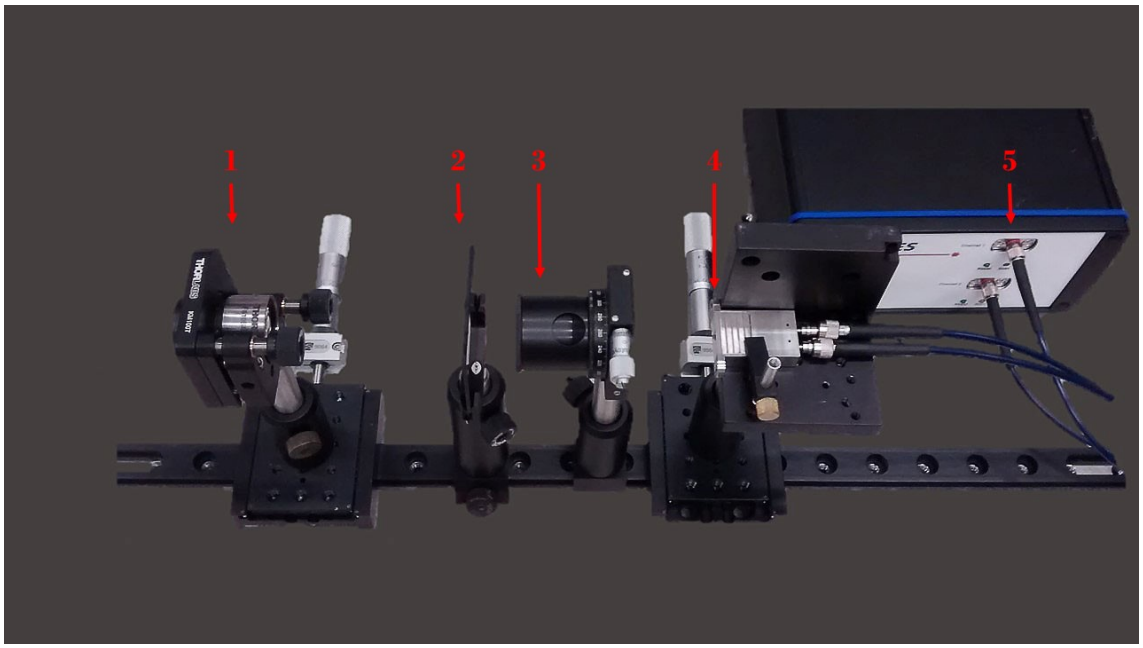

Figure 3.1: Instrumental Set-Up used for the calibration procedure. From left to right: the fibre carrying the light source collimated through the lens (1), the neutral density filter(2), the polarimeter (3), FlySPEX polarimeter (4) and the spectrometer featuring two entrances for the two channels (5).

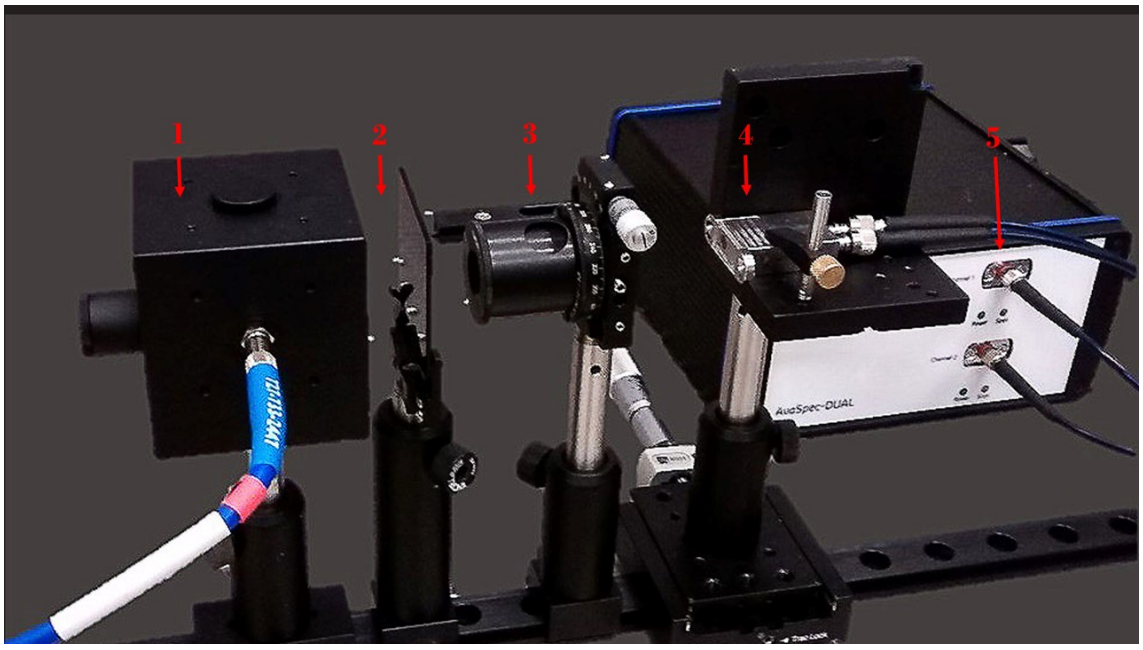

Figure 3.2: Instrumental Set-Up used for the calibration procedure. From left to right: the fibre carrying the light source inside the integrating sphere (1), the neutral density filter (2), the polarimeter (3), FlySPEX polarimeter (4) and the spectrometer (5) featuring two entrances for the two channels.

The second experiment was performed in order to acquire precise values of the extinction ratios of the beam-splitter manufactured for the polarization optics inside FlySpex. The element is described in [3] and consists of a cube with a dielectric splitter coating at the hypotenuse that creates the two channels with opposite polarization directions, and a triangular prism in contact with the splitter surface, that deviates the second channel, through

internal reflection, so that they become parallel to each other.

During the calibration analysis it appeared that one of the possible error causes could have been the inaccurate extinction ratio of the two channels of the beam-splitter, therefore an analysis of the single optical element was required in order to retrieve these parameters. To perform the experiment, 100 % polarized light in the $+Q$ and $-Q$ directions was used. A complete explanation will be presented in chap. (5) together with the results obtained.

The Set-Up is similar to the one used for the entire calibration, but an iris diaphragm has been used before the polarizer in order to limit cross talk between the two channels and stray light, and another one after the beam-splitter in order to select one beam only to be collected at the final lens. This lens is a collimator used to direct the light inside the fiber and inside the spectrometer.

The last three elements in Figure (3.3) are mounted on one-axis moving mountings, in order to allow a better alignment and to move the iris diaphragm and the collimator from one channel to another, since they are parallel at $\approx 11\ mm$ distance between each other. Figure (3.4) shows a schematic representation of the Set-Up: it is possible to notice how the moving platforms allow to retrieve at the detector the two beam, sequentially.

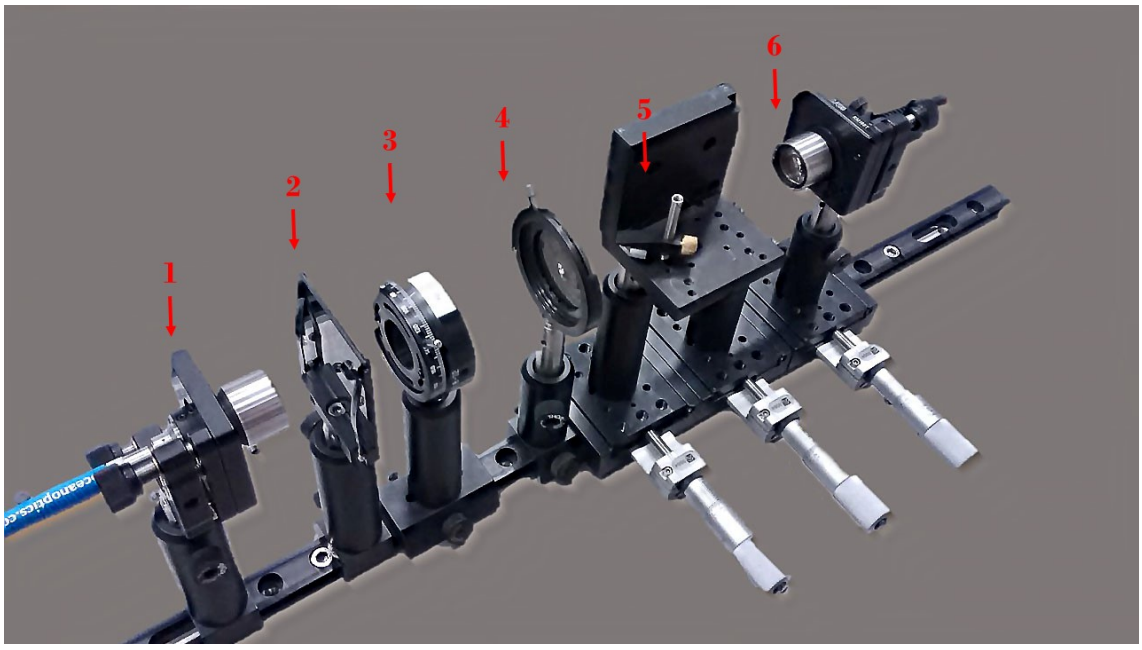

Figure 3.3: Set-Up used for the extinction ratios retrieval from the beam-splitter. From right to left: the collimator (1),the neutral density filter (2), the iris (3), the polarimeter (4), the polarimeter beam-splitter (5), another iris (6) and a second collimator (7) that conveys light through a fiber directly in the spectrograph. Three one-direction moving platform are used to align consecutively the first and the second beam coming out of the polarimeter beam-splitter.

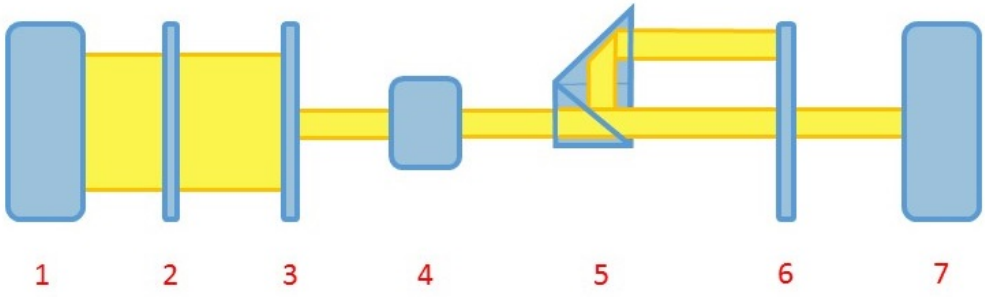

Figure 3.4: Set-Up used for the extinction ratios retrieval from the beam-splitter. From right to left: the collimator (1),the neutral density filter (2), the iris (3), the polarimeter (4), the polarimeter beam-splitter (5), another iris (6) and a second collimator (7) that conveys light through a fiber directly in the spectrograph. Three one-direction moving platform are used to align consecutively the first and the second beam coming out of the polarimeter beam-splitter.

4

NUMERICAL MODEL

Pages from 21 *to* 43 *are omitted in this version due to confidentiality issues*

4.1. THEORETICAL SET-UP

Pages from 21 *to* 43 *are omitted in this version due to confidentiality issues*

4.2. TRANSMISSION CORRECTION SIMULATION

Pages from 21 *to* 43 *are omitted in this version due to confidentiality issues*

4.2.1. EXTINCTION RATIOS

Pages from 21 *to* 43 *are omitted in this version due to confidentiality issues*

5

CALIBRATION

5.1. TRANSMISSION CORRECTION

Pages from 21 *to* 43 *are omitted in this version due to confidentiality issues*

5.2. CALIBRATION PROCEDURE

MOR RETARDANCE CURVE
DOLP EFFICIENCY CURVE
QWP CURVE CORRECTION

Pages from 21 *to* 43 *are omitted in this version due to confidentiality issues*

6

Data Retrieval

6.1. Fit Procedure

Pages from 21 *to* 43 *are omitted in this version due to confidentiality issues*

6.2. APPLICATION OF CALIBRATION CURVES

AOLP CORRECTIONS

DOLP CORRECTIONS

Pages from 21 *to* 43 *are omitted in this version due to confidentiality issues*

7

Conclusion Part I - Calibration & Data Retrieval Results

Pages from 21 *to* 43 *are omitted in this version due to confidentiality issues*

Part II:

Instrument Feasibility Study

8

INTRODUCTION TO PART II

In order to provide an accurate first level of a feasibility study for the implementation of the instrument in a small satellite space mission, two approaches will be used with the purpose of delivering a complete design.

The first approach will be a Bottom-Up method: beginning from the detector of the instrument, designed with an initial standard size, the design will then be expanded to the optical parts of the spectrometer (i.e. gratings, lens or mirrors) in order to lead to a general overview of the maximal performance of the instrument.

The second approach will consist of a Top-Down method instead: a general look at the common small-satellite sub-systems, their performances and sizes will give an insight on the possibilities and technological requirements for the instrument, e.g. size, power or viewing directions. These requirements, together with the scientific ones that drive the general instrument development, will be a starting point for the instrument design, that will be developed with increasing details. The research will start investigating the general instrument possible configurations, through the fibers orientations, spectrometer performances and then optical performances.

A comparison between the results from these two approaches and the general requirements will be carried out, and the results of this iteration will be presented. This process will constitute the main verification method.

8.1. SATELLITE STANDARDS

The miniaturized nature of FlySPEX suggests a possibility to be integrated as a payload of a small satellite mission, a procedure that could lead to an extremely cost-effective and standardized solution.

A market research reveals the extensive use in the past years of the CubeSat standards, vastly implemented for scientific missions and very compatible in terms of power, pointing and aperture size for passive sensor payloads ([33]).

A standard 3*U* is then selected, given the overwhelming presence in the small-satellite production with respect to the other standards, and also because of the availability of numerous platforms sold with already assembled modular subsystems that save development time and cost and maximize the payload space (data shown in Figure 8.2). According to [34], the 3U platforms are able to host up to a 2.3U payload size with a power supply up to 3.68 *W* and have a TRL of 9 (data for the GOMX platform developed by GomSpace ApS).

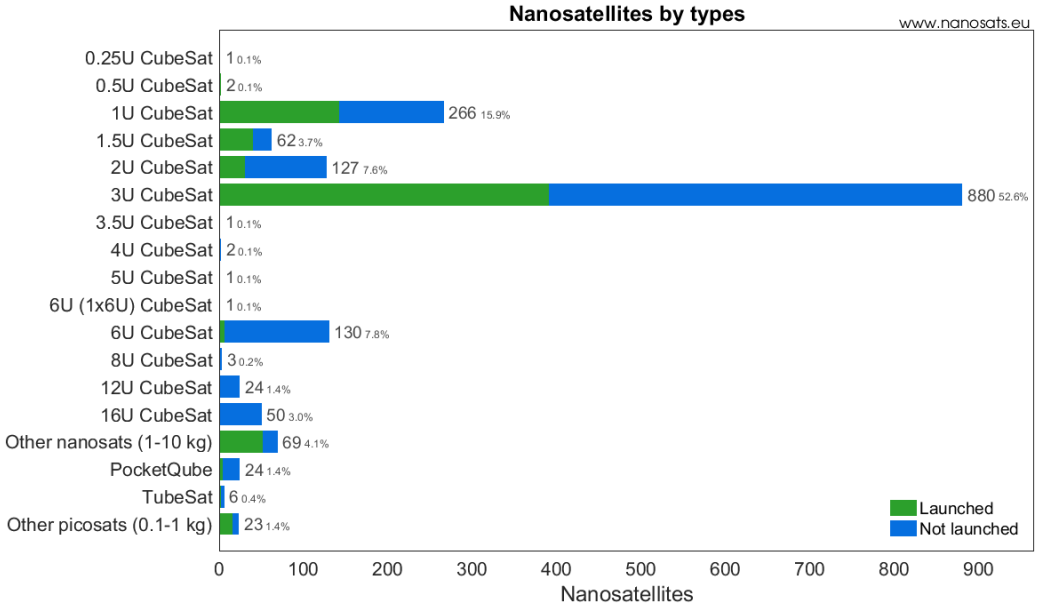

Figure 8.1: Updated statistics on types of launched/to be launched CubeSats. [35] Last update: 14-03-2017.

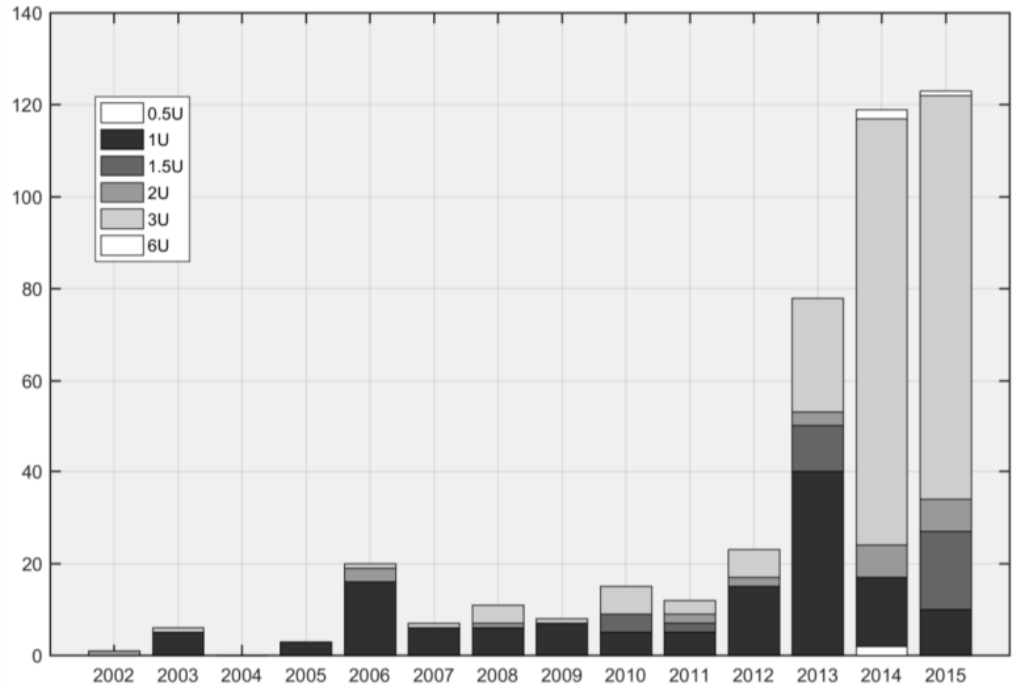

Figure 8.2: Figure from [1]. Statistical analysis of launched CubeSats.

From this standard the major technical constraints are derived, which are the payload dimension, the payload mass, the power available for the payload, the data rate allowed and the fiber-head configuration. These constraints are shown in table (8.1).

Technological constraints	
Structure	
SZ-001	The Payload shall only occupy $1U$ of the spacecraft, including microelectronics, thermal control units and BUS for power and data access.
SZ-002	The configuration chosen for the payload shall be able to stand high vibration phenomena present at launch.
SZ-003	The Mass of the entire spacecraft shall be below 4000 g.
Power Constraints	
PW-001	The instrument shall ask for an amount of power below 1.5 Watt.
PW-002	The voltage required for the instrument alimentation shall be 3 or 5 V, compliant with the CubeSat standards.
Data Constraints	
DT-001	The Data Bus shall be compliant to the I^2C protocol.
DT-002	The Data Rate of the instrument shall remain below $1000 bit/s$.

Table 8.1: Technological constraints imposed from the CubeSat standards [36].

9

BOTTOM-UP APPROACH

The Bottom up approach followed during this project is shown in fig (9.1) below. The design of the detector will be the starting point of this investigation, further expanding it to the spectrometer components, its general properties and finally the entire instrument.

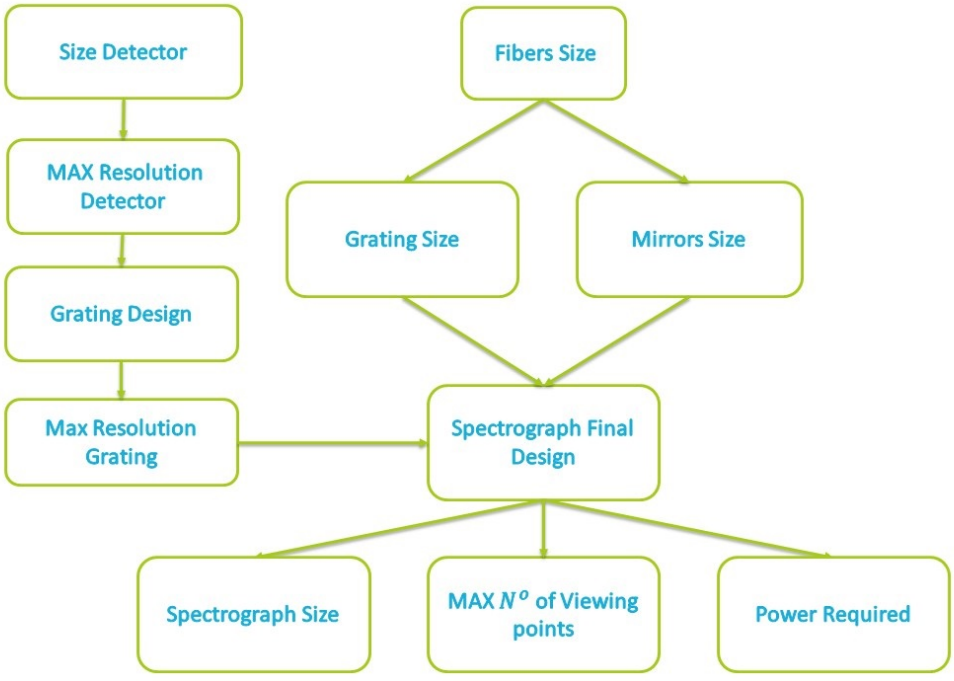

Figure 9.1: Concise representation of the essential step to be made to create the design of the instrument using a **Bottom-Up** approach. The starting point will be the choice of the detector, that will constraint the design of the diffracting elements and the lens or mirrors of the spectrometer. Once designed, the general performance of the instrument is retrieved and presented as a design result.

9.1. SPECTROGRAPH SELECTION

Spectrograph are widely used, with numerous purposes, from scientific investigation (astronomy, biology, physics etc.) to telecommunication. [37] reviews all the state-of-the-art spectrograph classes, to be implemented for future telescopes in order to improve the compactness, stability (fewer moving parts) and improve performances. These review is then very useful to discuss the best technology compatible with the FlySPEX instrument, since it

requires a compact and very stable spectrograph that primarily can fit in the CubeSat standard.

The reviews divides the spectrographs in different classes, that will be analyzed here in order to identify the possibility for FlySPEX. These categories are: direct detection, grating and phased array, Fabry-Pérot and cavities, Fourier transform spectrometer and direct detection.

Based only on the resolving power of the instruments (defined as $R = \frac{\lambda}{\Delta\lambda}$), direct detection can be excluded, since the maximum performance reachable is $R = 100$ while values for astronomical observation, in the visible domain, are typically higher. Fourier transform system are not considered an option for this instrument, since fringes created can interfere with the modulation pattern of the polarized signal, thus it may be troublesome to implement a similar device. Good options are then represented by grating and phased array, and Fabry-Pérot and cavities technology. These instrument can be characterized by their resolution and resolving power (defined in Section (9.3.3)) and another important parameter, the Technology Readiness Level (TRL). This parameter indicates the development level of a current technology, rating it from 0 to 10. In order to have a space-proven element, a TRL of 8 or higher is requested.

The first group refers to spectrograph that uses classical dispersing elements, like gratings and prisms. This category is the most used and currently the most sensitive [37]. While prisms always lead to bulky solution and a general increase of space, gratings are expanding their popularity given their compactness and the flexibility on the resolution obtainable [38].

Current new technologies are in development, and a system like Semi-integrated Compact Grating Spectrometer (CGS) can probably be very interesting for future development. This system is a combination of a double grating system in a non collimated beam and it is extremely compact (volume of the prototype 0.135 cm^3), reaching a resolution up to 3 nm and high enough resolving power (presented with all the detail in [39]). This technology is still new and not tested, thus it will not be considered during the feasibility study, but it can be selected in further development of the instrument.

Fabry-Pérot and cavities technology enable the separations of the wavelength through filtering the unwanted range (by reflection). Filtering results to be quite inefficient if the reflected light is not utilized, but some solutions allow high resolution and efficiency. Between these solutions notable are the Photonics Crystal Outcoupling Spectrometer (PCOS), that will be not treated here since it is still not space proven (TRL equals to 4), and MEMS-Based optical mini spectrometers (MEMS) that can be discussed, given their TRL of 8.

MEMS are systems that employ a tunable Fabry-Pérot technology on a micro-chip to allow the retrieval of spectra with a limited range and resolution. This technology appears to fulfill the requirement for an astronomical application and it is used in the visible and infrared spectral range, thus it fulfills the requirements for the FlySPEX instrument [40].

Between the technologies here presented, some new and advance spectrometer concepts can be very adaptable to future spectral observations, thus are cited here in order to give a

general overview. From this discussion it appears that classic gratings and MEMS can be the feasible concept at the moment for FlySPEX. Since the grating technology is currently vastly used and customizable, the following discussion will focus on that, in order to have a first estimation of the size and properties of this spectrograph. The MEMS option is cited in order to consider it as an off-the-shelf option for further development of the instrument.

9.2. DETECTOR DESIGN

9.2.1. CCD OR CMOS

The detector size is derived from the specification of the space qualified model STAR250 by Cypress, the selected detector. Its choice derived from its use for the SPEX instrument, where it was proven to be fully compatible with the instrument standards. Moreover, it is a readily available off-the-shelf product, ready and tested for a space mission, and its main advantage is the high resistance to radiation (up to a total radiation of 300 $Krad$).

As a general remark, the choice of the detector is very flexible at this stage of the design, since the only elements needed for the preliminary spectrograph design are the pixel size and the number of pixels. No specification are required on the typology of detector, that mainly distinguish between Charged Coupled Detector (CCD) and Complementary Metal-Oxide-Semiconductor (CMOS). These choice can be made later on during the design process, basing on performances (read-out speed, spectral range, Signal to Noise Ratio) and cost. The choice of the CMOS produced by Cypress is then just a starting point for the initial quantification.

Choosing this detector will directly determine the power used by the instrument, since this element is the only one requiring power. For the STAR 250 model, the power required correspond to 350 mW, 5 V. The detector comprise the Analog Digital Converter (ADC), but the micro-controller responsible for the payload operations is not comprised in this evaluation, future design will take that part into account. The power required is still expected to be much lower than the one required (1.5 W).

9.2.2. SIZING

The CMOS model mentioned before features 512 pixels, 25 μm wide each. The height of the spectra is the first quantity that has to be assessed: since the fiber is rounded, the detector will image a rounded element, thus the height will be equivalent to the width of the resolution element. The height of the spectra is then fundamental to assess the minimal resolution required from the spectrograph.

The instrument operational wavelengths go from 400 to 800 nm, thus the spectral range is assumed to be $S = \sim 400\ nm$. We also assume that the spectra will occupy a width of $W_{pix} = \sim 400$ of the total 512 pixels available, leaving the sides free. Given that, the required resolution $r = \Delta\lambda$ can be found as:

$$r = \Delta\lambda = \frac{S}{N^o_{el}} \tag{9.1}$$

with,

$$N_{el}^{o} = \frac{W_{pix}}{w} \tag{9.2}$$

where N_{el}^{o} is the number of resolution elements, w is the width of one resolution element (expressed in pixels), W_{pix} is the total number of pixel used and S is the spectral range.

Knowing the minimal resolution permitted at the CCD, it is important to continue the sizing process at the gratings in order to determine some fundamental properties for the spectrograph.

It will be important, in the last phase of the design, to make sure that the single resolution element completely contains the image, whose size will be determined by the other parameters in the spectrograph (diffraction limits of the mirrors, line spacing of the grooves in the grating, focal distances, etc.). For that reason, the size of the resolution element will be a key constraint for a first order design of the spectrograph.

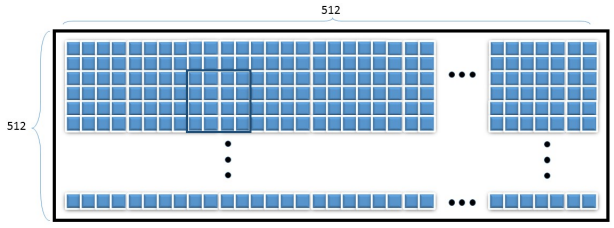

Figure 9.2: Schematic representation of the detector with 512x512 pixels (represented in light blue). The resolution element is chosen to be 4 pixel tall and, given the rounded shape of the fiber that is imaged, the width will then be 4 pixels as well. The resolution box is shown in dark blue, the three dots represent the repetition of the same elements. No distinction between CMOS and CCD detectors has been made.

9.3. DIFFRACTION GRATING DESIGN

9.3.1. PLANE VS CONCAVE GRATING.

Once a grating is selected, a decision on the shape is fundamental for the design of the entire spectograph, since the different existing categories (plane and concave) feature different mounts.

A plane grating has a flat surface and can be used in collimated (with its focus at infinite) light only, thus auxiliary optics need to be placed before and after the lens in order to first collimate and then focus the light on the detector.

A concave grating is a concave mirror with the ability to diffract light. The advantage of this element is that it provides focusing without the need of a separate element. A separate optical element will still be needed to collimate the light before the grating, not to have a straight focal curve imaged on the detector. Nevertheless, new classes of concave gratings with varying groove patterns can receive light from a point source and image on a focal curve

which is nearly linear (flat-field spectrometer, [38]).

In this discussion, we chose to design the spectrometer with a plane grating, since it offers different advantages: the absence of astigmatism aberrations in the grating, a simple design and large alignment tolerances (due to the collimated beam) [41].

9.3.2. GRATING MOUNTS.

The mount of a grating comprehends all the auxiliary optics that modify the angular configuration of the instrument and the wavefronts.

In this work only the mounting with mirrors will be discussed, given their major compactness with respect to lenses and the fundamental properties of having no chromatic aberrations (even though they will still show astigmatism and coma aberrations). The main mounting designs present in literature (e.g. [38], [42],[43]) are the ones shown in Figure (9.3).

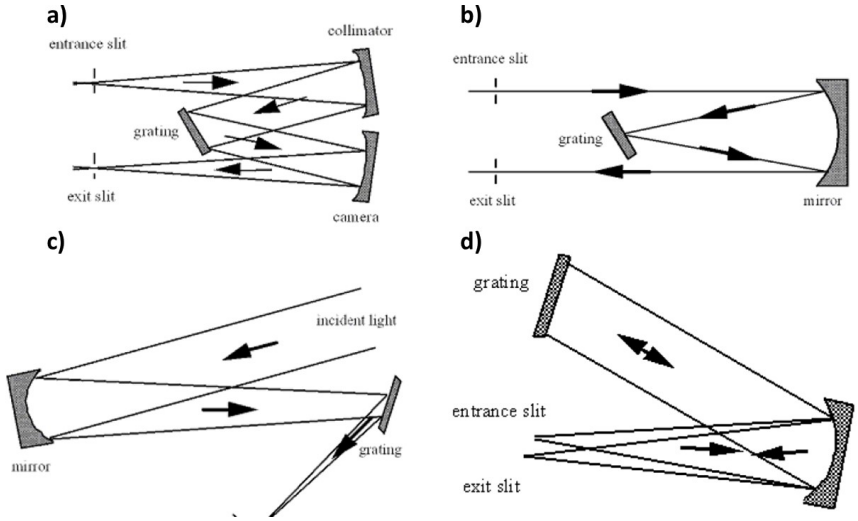

Figure 9.3: Different Spectrometer designs for a plane grating. a) Czerny-Turner mount, b) Ebert mount, c) Monk-Gillieson mount, d) Littrow mount. Figures from [38].

The simplest mount is the Monk-Gillieson (Figure 9.3c) since it is formed by a converging beam that passes through a mirror and a grating to be imaged in the exit slit. This configuration is very simple and cheap to realize, but it introduces wavelength-dependent errors due to the non-collimated light at the grating, therefore nowadays it is just used for very low-resolution applications.

The Littrow configuration (Figure 9.3d) is very popular since, reflecting at the same angle, can provide the maximum attainable resolving power [38]. This configuration is not used here because of the too small off-set created between the entrance and exit slits, that will not allow for a physical assembly of fibers and detector. This off-set introduces also additional out-of-plane aberrations.

The Czerny-Turner spectrometer (Figure 9.3a) is a configuration that directs collimated light to the dispersing element (the grating) and then refocuses the beam at the exit slit (through the mirror called camera in Figure (9.3a)). Aberration will then only be introduced

by the mirrors (spherical mirrors are often used, leading to spherical aberrations).

The Eber-Fastie design (Figure 9.3b) is a special case of the Czerny-Turner, that uses only one mirror as a collimator and camera. The fabrication of such a mount is easier than the Czerny-Turner and all the misalignment errors of camera and collimator are avoided, even though aberration and stray-light are more difficult to control due to the reduced design parameters.

Between these options, the one chosen is then the Czerny-Turner since it allows for a better control of aberrations, more degrees of freedom in the design (compared to the Eber-Fastie) and a compact design.

9.3.3. GRATING KEY PARAMETERS.

The key elements for the design of the diffraction grating are the groove frequency (the number of lines per mm requested in the grating) and the inclination angles α and β as defined in figure 9.4.

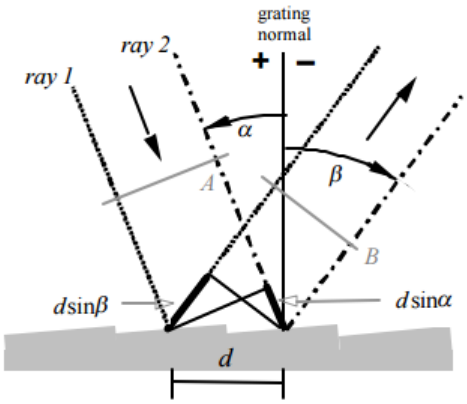

Figure 9.4: figure from [38], α and β are the angles of the incoming and reflecting ray respectively, taken from the normal to the grating plane. The figure shows the principle of the grating on two incident rays, that are in phase if the difference of their path lengths $dsin\alpha + dsin\beta$ is an integral number.

From the resolution computed beforehand, it is possible to obtain the resolving power of the grating and the linear dispersion, knowing the following relations:

$$R = \frac{\Delta\lambda}{\lambda} \tag{9.3}$$

$$\frac{dl}{d\lambda} = \frac{w'}{\Delta\lambda} \tag{9.4}$$

where R is defined as the grating resolving power, w' is the slithwidth corrected for anamorphic magnification and spectral magnification, in this case corresponding to the spectra width imaged on the detector, and $\frac{dl}{d\lambda}$ is the linear dispersion of the element. The angular dispersion A can then be obtained as:

$$A = \frac{1}{\frac{dl}{d\lambda} f_{cam}} \tag{9.5}$$

where f_{cam} is the focal length of the camera optics, here assumed to be equal to the focal length of the collimator. The groove spacing d is defined by the illuminated lines and the width of the grating. The illuminated lines can be obtained from the relation:

$$R = Nm \tag{9.6}$$

where N is the number of lines and m is the order of the grating. The order m is here assumed to be 1, since it avoids the overlapping problems of different order dispersion: as defined in [38], the free spectral range is, in fact, $F_\lambda = \frac{\lambda}{m}$, where λ is the smallest wavelength in the considered range. Since our range starts at $400nm$, in order to have a free spectral range until $800nm$, m should be equal to 1.

If we then assume that the angle β presented in Figure (9.4) is at -55^o with respect to the normal to the grating plane. It will then be possible to retrieve the required line spacing d and the angle α using respectively the formula of the angular dispersion and the general grating formula, presented in eq. (9.7) and (9.8).

$$A = \frac{\lambda}{dcos(\beta)} \tag{9.7}$$

$$m\lambda = d(sin(\alpha) + sin(\beta)) \tag{9.8}$$

9.3.4. SPECTROGRAPH SIZES COMPUTATION

In parallel to this computation, analysis on the other end of the spectrograph needs to be performed, in order to generally retrieve the dimensions of the single optical elements.

One known element is the numerical aperture of the optical fiber, that always come as a specification of the selected fiber and was chosen to be $NA = 0.22$ [3]. From this value the $F\#$ (F number, defined as the focal length over the diameter of the element) of the optical fiber can be retrieved, since, according to [44]:

$$F\# = \frac{f}{D} \sim \frac{1}{2NA} \tag{9.9}$$

Knowing that the collimator and the optics before it (in this case the fiber) need to have the same $F\#$, we have that:

$$\frac{f_{fiber}}{D_{fiber}} = \frac{f_{coll}}{D_{coll}} \tag{9.10}$$

From this expression it is possible to retrieve the values for the diameter of the first mirror, which is the collimator, assuming a fixed focal length for the mirror (in this case a 2.5 cm focal length has been chosen for compactness).

Assuming that a collimated beam is received by the grating, then the same dimension can be assumed for both the elements.

The dimension of the camera can be assessed by roughly knowing the dimension of the cone of light created by the grating. This light will still be collimated but dispersed by the grating, so the camera diameter is expected to be larger than the grating diameter. In order to compute its dimensions we need to roughly estimate the aperture of this cone of light,

thus the dispersion angle β is computed for the wavelengths at the extreme of our spectral band, respectively 400 nm and 800 nm using formula (9.8). These two values indicate the total dispersion of the light cone and lead to the dimension of this cone at the camera, using the following formula:

$$D_{cam} = D_{coll} + l * tan(\beta_{800\ nm} - \beta_{400\ nm}) \tag{9.11}$$

where l is the path from the grating to the camera followed by the light at $\lambda = 600\ nm$ (the wavelength in the middle of the spectral range) that is found, once the height distance between the grating and the camera h_2 is known, as $l = h_2/sin(\beta)$.

The value we need to establish now is the height of the system, from which we can asses the height between collimator and grating, h_1, and grating and camera, h_2, that will lead to know the dimensions of the camera.

Nevertheless, the total height of the spectrograph H cannot be lower than the sum of the camera and collimator mirrors or the height of the aperture plus the grating and the detector, otherwise, referencing to the chosen mounting (Czerny-Turner in figure 9.3) they will have to overlap with each other.

Since the spectrograph height and the camera diameter are both unknown and linked by the mathematical relations shown before, iterations have to be performed to assess these two parameters. The process is illustrated in figure (9.5).

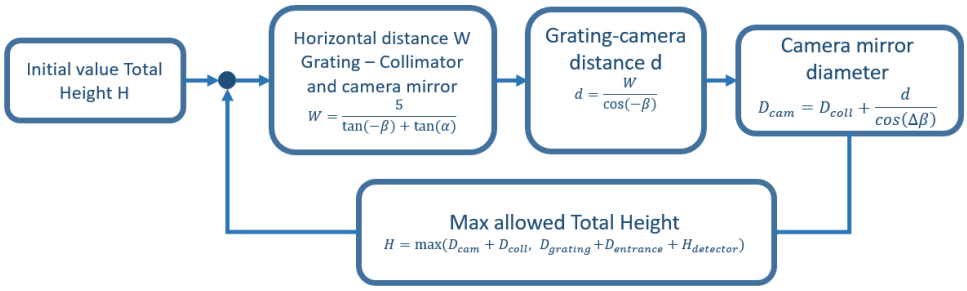

Figure 9.5: Visualization of the iteration performed to assess the spectrograph height and camera mirror diameter.

This first order analysis will help to know what the expected size of our spectrograph is and it will be a first step for the assessment of the feasibility of the mission.

To conclude, a more detailed and in depth analysis is necessary for spectrometer characteristic values here presented to be optimized. For this process a specific optical software needs to be used, while the values here mentioned will be a good initial guess for the design, accurate enough to assess the feasibility for this primary study. A software as Zemax OpticStudio can be ideal for this type of process.

Table 9.1 shows the results computed using the formulae described in this section. A first sketch of the spectrograph is presented in figure (9.6).

Spectrograph Design		
Assumptions		
Resolution Element	$[pixel]$	4
N# of pixels	$[pixel]$	4
Spectral Range	$[nm]$	400
grating order	[-]	1
Pixel length	$[\mu m]$	25
Focal length Collimator	$[cm]$	2.5
Focal length Camera	$[cm]$	2.5
Angle β	[deg]	-55
Spectrometer vertical height	$[cm]$	4.4
Fibers Numerical Aperture NA	[-]	0.22
Results		
N# resolution elements	[-]	100
Resolution	$[nm]$	4
Resolving Power	[-]	150
N# of lines	[-]	150
1/linear Dispersion	$[\text{Å}/mm]$	400
Angular Dispersion	$[rad/\mu m]$	1
groove spacing d	$[\mu m]$	1.7434
line frequency	$[lines/mm]$	573.57
Angle α	$[deg]$	66.652
F#	[-]	2.27
D_{coll}	$[cm]$	1.1
$W_{grating}$	$[cm]$	1.1
Angle β_{800nm}	$[deg]$	-27.34
Angle β_{400nm}	$[deg]$	-43.53
D_{cam}	$[cm]$	1.695

Table 9.1: Spectrograph design parameters.

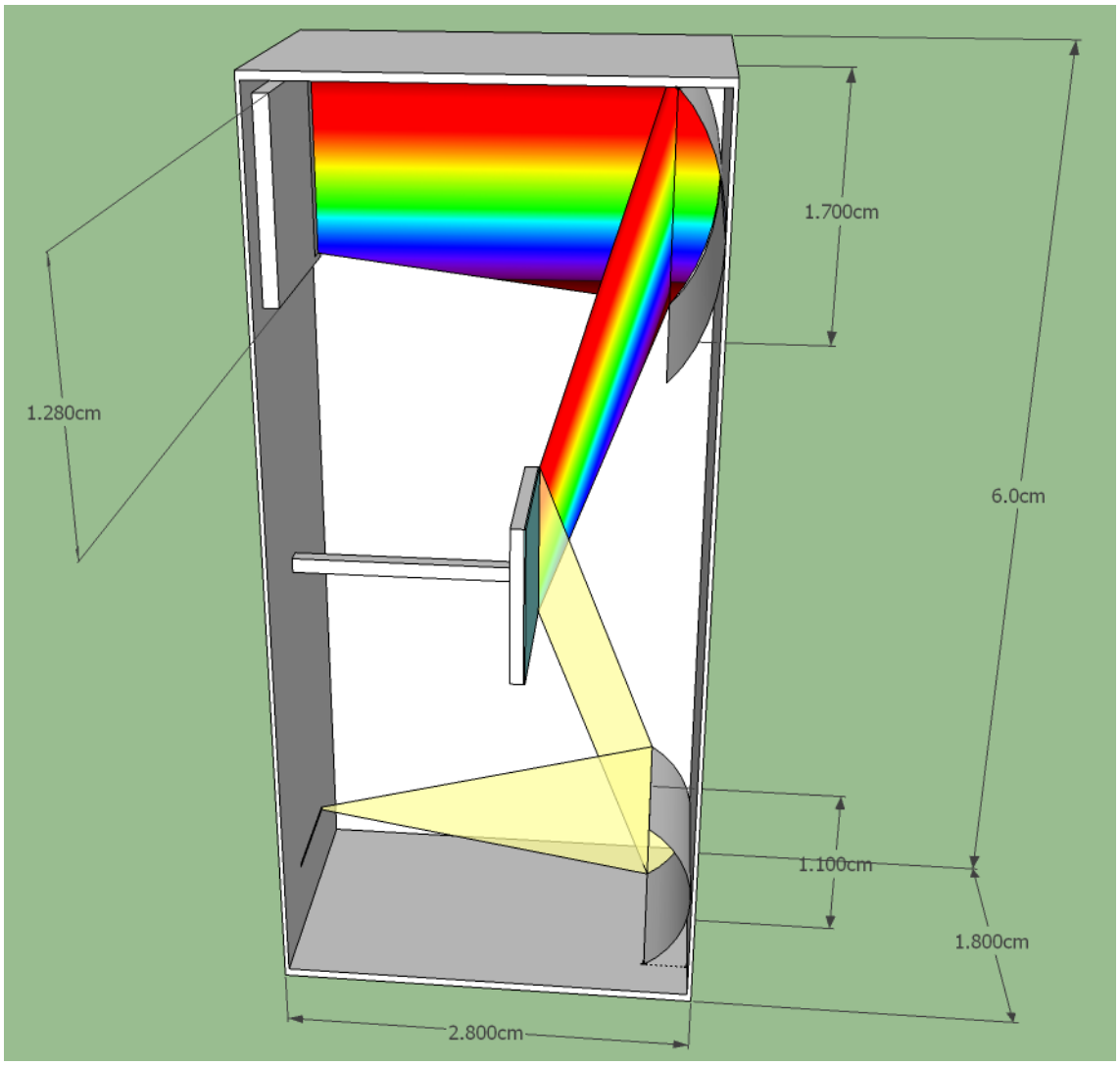

Figure 9.6: Impression of the first arrangement and dimensions of the spectrograph. Entrance of the ~ 40 beams at the lower left, only one is represented for clarity. The beam then encounter the first mirror that collimates and reflects the beam into the grating, the element in the middle, that disperse the beam into the second mirror, the camera, that image the dispersed beam into the detector, the last element on the upper left.

9.3.5. NUMBER OF FIBERS ON THE FOCAL PLANE

The assumption of maintaining the focal lengths of collimator and camera equal results in an easier design of the spectograph and also in a 1 : 1 ratio between the slit width and the width of the detector.

This consideration is useful for the computation of the maximum number of fibers that can be connected to the spectrometer and can produce a spectrum on the detector. We considered that at the detector 1 pixel length is 25 μm and that one spectrum is 4 pixels high. We also consider that we are leaving margin at the extremities of the detector, thus, we assume to use only 400 pixels out of the standard 512, in order to avoid the typical transmission drop at the boundary of the detector. Therefore, leaving an equivalent space of four spectra between two different spectral line, the maximum number of allowed spectra at the detector will be 50. If a more conservative approach is used, leaving a space between the spectra of 6 pixels instead, then the spectra allowed at the detector will be max 40.

This first order computation is very useful in order to find how many fibers can be plugged in in the focal plane (or slit) of a single spectrograph. Given that each viewing direction images 2 spectra, then the maximum viewing points are 20, using the more conservative approach.

10

TOP-DOWN APPROACH

To adapt FlySPEX for a space mission using a top-down approach, the starting point is the analysis of the requirements, derived from the scientific objective of the mission.

The objective of the mission will be remote sensing of the Earth atmosphere with a multi-angle, multi-wavelength snapshot innovative technology to allow for a precise retrieval of aerosols properties.

The paper by Hasekamp [12] demonstrated that, if provided with sufficient viewing angles and high polarimetric accuracy ($0.002 - 0.004$), the instrument may be also capable of retrieving cloud deck properties (i.e. cloud effective radius, effective variance, droplet number concentration and cloud fraction). This objective is not fundamental but will be taken into account for the instrument design. The main scientific requirements, needed to assure the quality of the retrieved data, are listed in table (10.1).

Scientific Requirements	
Spectral Requirements	
SP-001	The spectral range of the instrument shall be inside the visible-NIR spectrum.
SP-002	The spectral resolution of the instrument shall be higher than the polarimetric modulation period along all the spectra.
Attitude Requirements	
AT-001	The orientation of the Spacecraft shall be known with an accuracy of **TBD**.
Coverage Requirements	
ST-001	The instrument shall not be mounted on any movable platform such as scanners.
ST-002	The Ground Object Length of the instrument when nadir pointing shall be **TBD** long.
ST-003	The Field of View (FOV) of a single viewing point shall not be lower than 1^ox1^o.
ST-004	The viewing points shall not be less than **TBD** in the along-track direction.
ST-005	The viewing angles in the along-track direction shall be at interval of **TBD** deg.
ST-006	The instrument shall be able to cover the same scene at least once a day.
Polarimetric Requirements	
PL-001	The Polarimetric accuracy shall be equal or better than 0.1.
PL-002	The Polarimetric spectral resolution shall allow to obtain at least one polarimetric value for the blue, green and red part of the spectra.

Table 10.1: Scientific Requirements list.

As it is possible to notice, some fundamental requirements are not quantified (hence the "To Be Determined", **TBD** acronym). Objective of this part of the thesis is trying to quantify the required quantities and derive a possible design solution beginning from them and from the technological constraints presented in Table (8.1). This work will give a better insight on the expected spacecraft orbit, expected attitude accuracy and expected viewing points configuration.

Once this is done, a clear idea of the required configurations of the viewing points inside the CubeSat can be inferred and from this, the space remaining for the spectograph is obtained. This value will then lead to final considerations about the expected nature and performances of the spectrometer as for resolution, power required, and data rate requested. In order to clarify the main passages of the design here presented, the block diagram below has been developed.

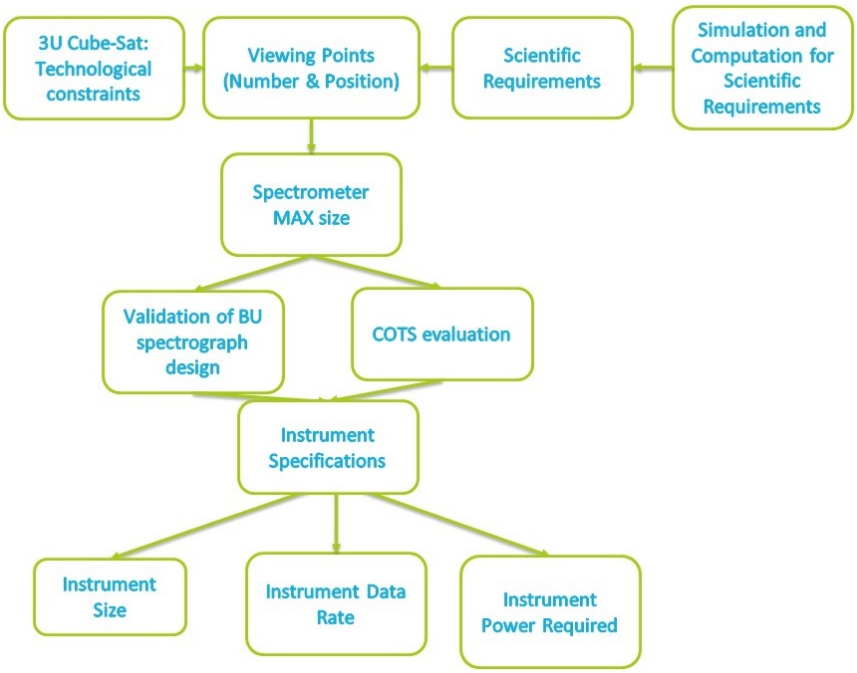

Figure 10.1: Concise representation of the essential steps to be made to create the design of the instrument using a **Top-Down** approach. The scientific requirements and the available space for the payload in the satellite will represent the constraints of the design of the instrument, this will give a hint on the spectrometer maximum performances and a first estimate on the real resolution of the spectrometer, made through an evaluation of COTS present in the market and a customized spectrograph design. As for the Bottom-Up, the results are the general performances of the payload that will be used as input for the other subsystem design.

10.1. DISCUSSION ON REQUIREMENTS

10.1.1. ATTITUDE REQUIREMENT

This is a fundamental requirement for the assessment of the quality of the scientific data produced from FlySPEX: its ability to keep the track of one point on the ground is fundamental in order to provide multi-angle information of the aerosol particles present in a region.

Pointing accuracy represents the attitude error of the spacecraft with respect to the designated target and it is the fundamental parameter to be assessed to complete the require-

ment.

CubeSat performances greatly improved in the last year regarding Attitude Determination and Control: in 2011 the leading performance was recognized to the Canadian Advanced Nanospace eXperiment (CanX) [45], reaching a pointing accuracy better than 2^o. The last presented reviews [33][34] show a big improvement regarding this subsystem performances: state of the art integrated units (that combine multiple elements such as actuators and sensors into a single part with the aim to provide a simple, single component solution for Guidance Navigation and Control, GNC, requirements) can reach now pointing capability up to 0.007 deg occupying as little as $0.5U$ in the spacecraft (mass of 0.91 Kg)[46, Blue Canyon tech., Xact Unit]. Pointing error depends only weakly on the viewing angles of the spacecraft, thus how close to the horizon we are observing [44, p.130]. This leads to a very initial estimation of the pointing accuracy required for the spacecraft.

If we estimate the pointing accuracy with the only purpose of keeping at least one target always inside the field of view, then a virtual certainty will be obtained if the distance from the center to the border of the field of view corresponds to $FOV/2 = 6\sigma$. The pointing accuracy, usually estimated with 3σ, will then be $3\sigma = FOV/4 = 0.25\ deg$. Illustration in fig (10.2a) illustrates this geometrical consideration.

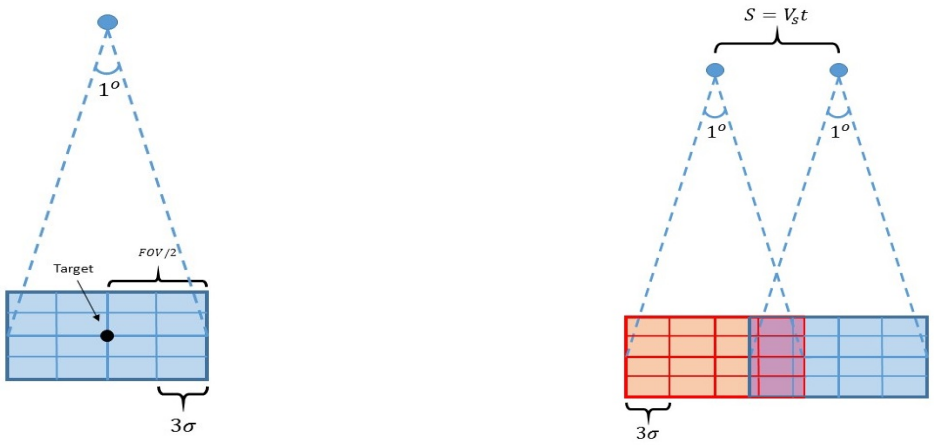

(a) **(b)**

Figure 10.2: Geometrical scheme applied for pointing accuracy requirement study. First order estimation of the pointing accuracy based on two different geometrical approaches. a) calculated accuracy based on the assumption that the target is ideally centered. The expected attitude uncertainties (3σ) still allow the target to be inside the FOV ($FOV = 1^o$). b) The second approach requires two consecutive images to have a continuous coverage. This objective is fulfilled if the images are taken with a distance S equal to the instrument FOV minus the uncertainties (3σ).

On the other hand, a more stringent requirement is obtained if we want to obtain a continuous coverage on the ground without overlapping of the pictures. In order to reach this objective, two consecutive exposures need to have a spacing d equal to the field of view size minus the pointing error. Figure 10.2b illustrates geometrically this condition. This implies that increasing the pointing accuracy will lead to a larger spacing between consecutive pictures, thus a larger covered area for a given number of pictures (less picture taken per time unit).

According to [44, p. 130], the ideal range of pointing accuracy in order to diminish the image overlapping is between 20 % and 10 %. A lower level will only slightly increase the overall coverage. For this reason, we finally assessed the requirement on coverage to the more stringent value of 0.1^o, being the 10 % of our FOV, and lower than the one assessed with the first consideration.

As it is possible to notice, current state-of-the-art technology can deliver almost a 2 magnitude order better accuracy than our current requirement. The GNC system is then believed to be not a killing requirement for our payload design, and the spacecraft will be assumed from here on to be virtually perfectly stable.

10.1.2. COVERAGE REQUIREMENTS

One of the main constraints for a remote sensing mission is the type of orbit that the satellite will follow. Its parameters (altitude, inclination, eccentricity, node) will directly affect the performance of the satellite (such as coverage, repeating time, swath width, resolution on the ground, etc.). Orbit design requires numerous iterations and it is highly influenced on the other sub-systems requirements: general indications are shown in this work in order to have some preliminary estimations. As stated in [44], one of the fundamental parameters to assess is the orbit altitude, since it greatly influences the payload performances. A first estimation has to be performed supposing a circular orbit.

In order to assess the altitude value some considerations are done, specifically addressing the peculiarity of this type of mission and creating a reasonable range of values for the altitude parameter:

- Coverage of the same scene at least once a day has to be granted, giving a constraint on the maximum altitude.
- Low earth Orbits (LEO) below 600 km are strongly affected by atmospheric drag, that reduce drastically the satellite's operational lifetime (altitude lower than $\sim$ 300 km will not be considered, having a lifetime lower than 1 year) [44, p.210].
- CubeSats are not radiation hardened thus they are designed for orbits in Low Earth Orbit, well below the Van Allen belts (altitude less than 1000 km).
- CubeSats are exclusively launched as second payload of a principal mission, thus a large flexibility is required during the design process, so that changes can be performed if launch opportunities arise.

These considerations are already limiting the altitude range of possibilities, that is clear to be from 400 km to 1000 km.
In order to have a more precise idea about the key orbit design parameters, altitude and inclination, a wide research on the characteristic of 3U CubeSat orbits is performed, so that a conclusion can be reached. Figure 10.3 shows a market research performed on mostly all the published orbits of 3-unit CubeSats that reached the operational status.

It is noticeable how the two most used orbit classes are the ones that belong to the ISS or are typical of the Sun Synchronous Orbits (SSO). Also considering that a higher spatial resolution for the instrument is obtained at low altitudes, the selected altitude range of our spacecraft will be around the two peaks shown in the figure, thus from ~ 400 km to around ~ 600 km.

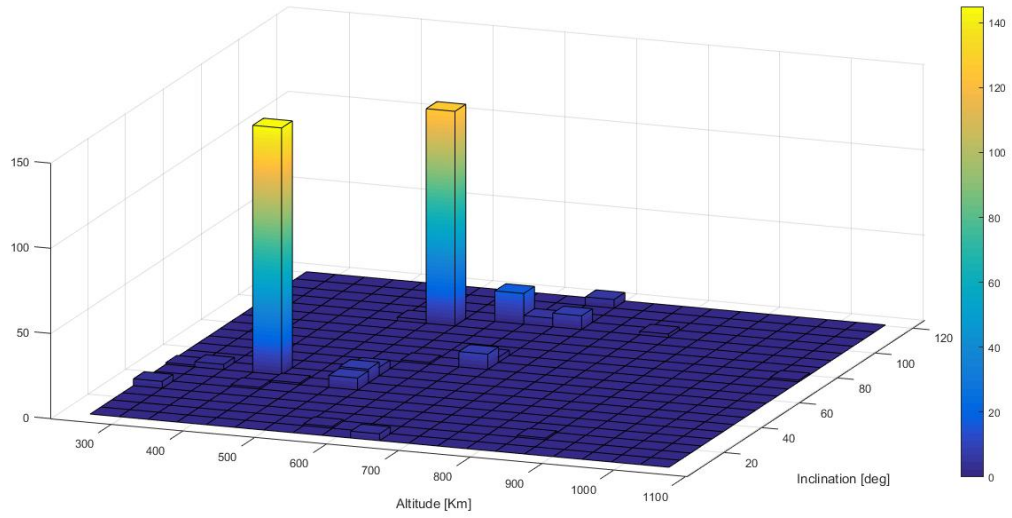

Figure 10.3: Market research on 3U CubeSat orbit parameters. The database [35][47] shows only the orbits for the 3U CubeSat class, which have reached the operational status. The numerous satellites that are grouped around 400 Km at 51.6^o of inclination are the ones launched from the International Space Station (ISS), since the station itself has that orbit. The second large group is constituted by Sun-Synchronous Orbits (SSO) around 500 – 550 Km and with an inclination of ~ 98^o.

GROUND OBJECT LENGTH

The orbit altitude directly leads to assess the swath width, since we already know that the instrument FOV will be $\theta_{FOV} = 1^o x 1^o$. For an altitude of $H = 400\ Km$ the swath width will then be $SW = 2Htan(\theta_{FOV}/2) = 7\ Km$, while, for $H = 600\ Km$ then $SW = 10.5Km$.

Figure 10.4 shows the relation between the optical payload in the spacecraft and the illuminated area on the ground. From that illustration it is possible to notice the relation between the detector size and the ground object area, and the pixel size and the ground pixel size. In order to estimate the equivalent size of a pixel on the ground, knowing the total illuminated area on the ground, it is necessary to know how many pixels this area occupies on the detector.

In order to know that, the design should delve more into the spectrometer properties. Assuming that the instrument entrance slit size is the size of the entrance fiber in the spectrometer, thus 100 μm, and assuming that the exit slit will have the same size (given that the optical focal length is maintained constant), then the size of the ground sample at the detector will be of 100 μm as well, occupying 4 pixels (since one pixel of the selected detector is 25 μm). The pixel size on the ground will then be 1/4 of the total ground object length, thus corresponding to 1.75 Km and 2.62 Km for altitude of 400 Km and 600 Km respectively.

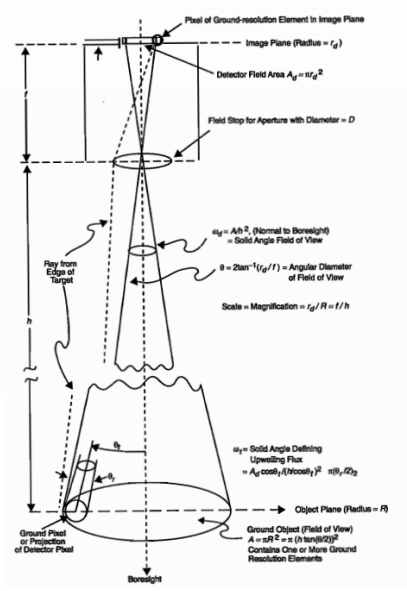

Figure 10.4: representation of the terminology used to indicate general payload design parameters. Correspondence between the detector size and the ground imaged area.

VIEWING POINTS

The Sun position with respect to the spacecraft is a main constraint and has to be optimized, being the payload a passive instrument that needs to receive scattered light at different angles, in order to return widely useful scientific data.

The scattering angle was defined in Section (1.2.1). It can also be defined starting from the phase angle, the angle between the Sun, the object and the observer. Defining this angle as Φ, then the scattering angle is $\pi - \Phi$.

The scattering angle will be the main constraint regarding the scientific quality of our observation. The type of orbit is then fundamental in order to assess the range of scattering angles that the instrument will be capable to retrieve. In order to develop a first study about the orientation, number and disposition of the viewing points, a Sun-Synchronous orbit is chosen at an altitude of 550 km, that passes the ascending nodal point at a local 12 AM. This way the scattering angle will be 180 degrees at 12 AM every day, ensuring that the final scattering angle range is the largest possible. Appendix (C) shows the case for the opposite case, when the scattering angle range is at minimum, thus when the orbit is a so-called *twilight* orbit, having the satellite passing the nodes around 6 a.m. and 6 p.m. local solar time.
In order to simulate variations during the whole year, caused by the latitude of the Sun with respect to the Earth equatorial plane, three convenient days have been chosen, corresponding to: the highest point (northern summer solstice, 21^{st} June 2017, when the Sun's latitude is 23.5^o), the latitude point of the Sun (which corresponds to the northern winter solstice, 21^{st} dec 2017, when the Sun's latitude is -23.5^o), and finally the time where the Sun is at 0^o latitude, on the equinox (northern spring equinox, 20^{th} March 2017). These points are indicated in the following discussion and figures as Summer, Winter and Spring.

Figure (10.5) shows the Sun-Synchronous Orbit selected for the simulation on the three different days, in order to highlight the changes in the Sun position.

Figure 10.5: Representation of the Sun-Synchronous orbit (SSO) chosen for the simulation during the 3 chosen days. It can already be estimated from this representation that this orbit maximize the possible scattering angles that can be retrieved, since the satellites starts close to the horizon and crosses the line that connects Sun and Earth, delivering data at 180^o scattering angle.

Once the orbit is simulated, the developed tool analyzes only the orientation of the Sun-Earth vector with respect to the pointing vector when the satellite is in illumination time. A typical illumination time for an entire day is shown in Figure (10.6).

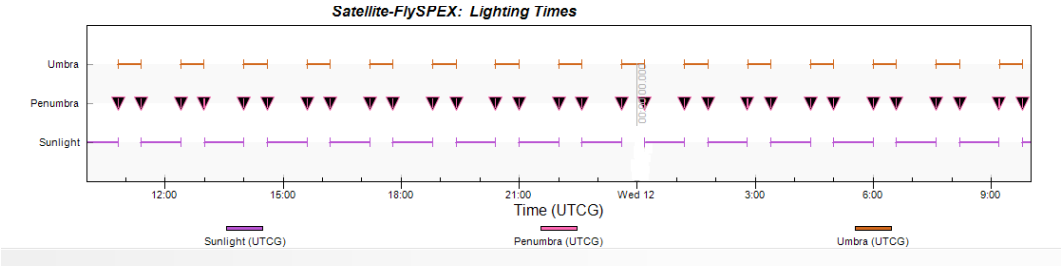

Figure 10.6: Simulation of the lighting time for a simulation for 24 h. The figure shows the interval where the satellite passes region illuminated by the Sun. the time used is the universal coordinated time UTCG with respect to the zero meridian.

Each viewing point will have a vector associated to it that will form a particular scattering angle with the Sun, thus a set of viewing angles has to be decided for the simulation, in order to distinguish the best performance.

In this work, four configurations for the viewing will be shown, that will serve as a primary assessment of the dependence of the scattering angles on the various configurations. The four configurations are shown in Figure (10.7), which is a bottom view of the spacecraft that indicates the beam coming out of the viewing directions with different colors.

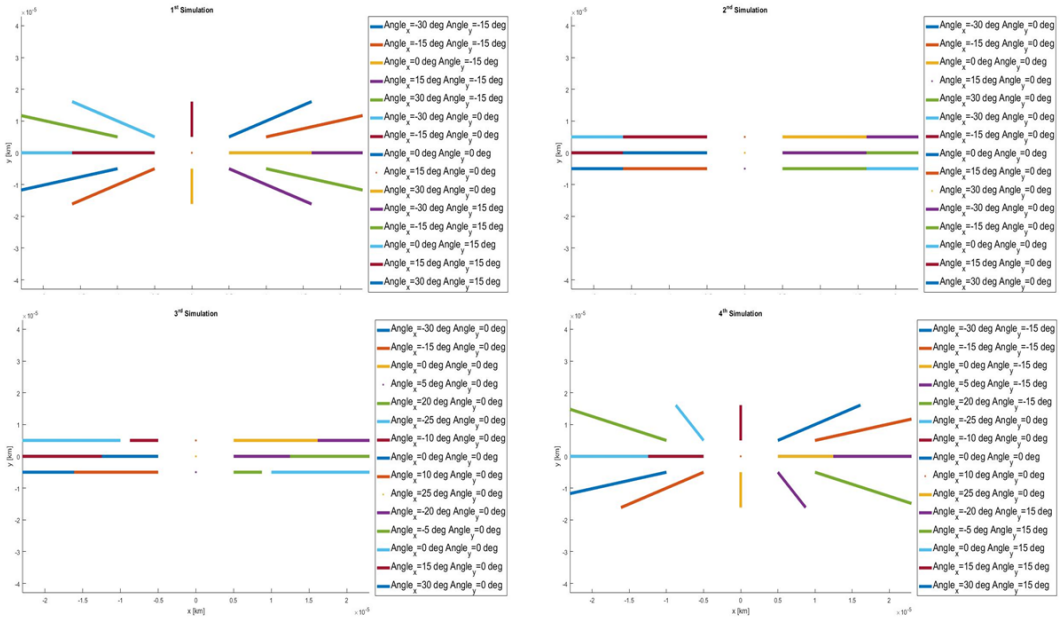

Figure 10.7: Bottom view of the four combinations used to perform a simulation for the scattering angles detected by the spacecraft. The x-direction indicates the along track axis (where the spacecraft velocity vector is oriented) and the y-axis is the cross-track direction. every configuration features three lines of along track direction with five viewing points each. The coloured lines represents the beams, as seen from a viewer placed at the nadir. each viewing point has its on inclination with respect to the x and y axes, as reported in the legend.

These configurations vary from each other regarding the angle on the x and y directions (directions referred to the spacecraft reference frame, with z pointing earth and x in the velocity direction). Summarizing, the configurations are:

1. symmetric for both x and y angles.
2. aligned along the y-direction and 15 degree angle step between the in-line viewings.
3. aligned but with variable angle step between the in-line viewings.
4. variable angles both in the x and y directions.

The scattering angle is computed from the scalar product of the Sun vector and this viewing vectors.

Figure (10.8) shows the results of this simulation for the four different configurations. The viewing points aligned along the velocity vector of the spacecraft (along-track) are here represented as an individual line.

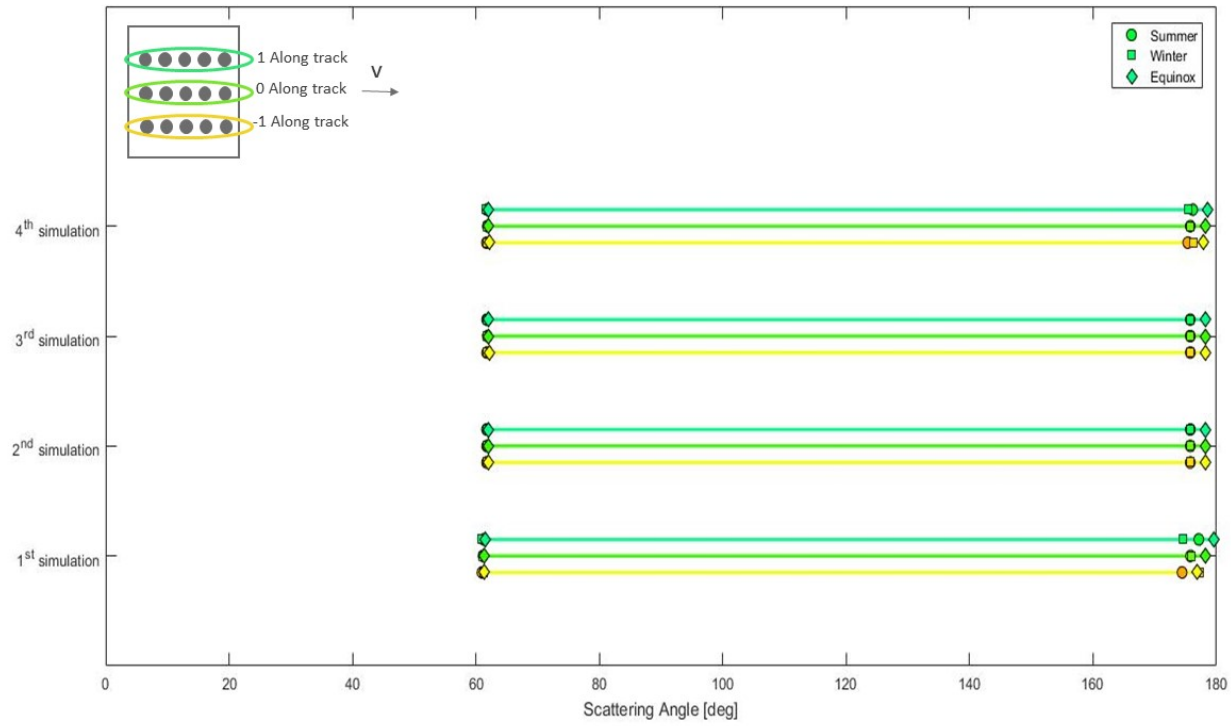

Figure 10.8: Results of the simulation of retrieved scattering angles during a $24h$ orbit in an generic Sun-synchronous orbit that passes its nodal point at 12 AM local time. Three days are displayed in the plot. The 21^{st} June 2017, the summer solstice, is called summer is represented with a circle at the extremities of the scattering range. In the same way, the 21^{st} December 2017 is the winter solstice, represented with squares and called winter in the legend. The 20^{th} of March, the spring equinox is called equinox in the legend and represented with rhombus. A little legend above on the right represents the viewing points of the spacecraft with the colour as represented in the plot in the 4 different configurations.

From the simulation results it is possible to notice how this particular SSO covers a wide scattering angle range, independently from the different along track lines of viewing points (that look at different region, represented in the figure with different colours). The range covered by this simulation completely fulfill the scientific requirement mention before, that ask to cover specifically the scattering region around 140^o. This region has a fundamental peculiarity: the rainbow phenomenon originated from internal reflection of light inside the particles [18]. This phenomenon creates a local maxima visible degree of linear polarization and slightly in the phase function (which is the the first element of the flux vector, previously defined as the intensity I,). These results are clearly visible in Figure (10.10). The originated peak is called primary rainbow, since it is created by a single internal reflection of light inside the particles. These rainbow feature is a clear indicator of the refractive index (composition) and shape of these particles and slightly on their size (if considered spherical, it can lead to an estimation of the effective radius r_{eff}) [48] [49].

It is important to notice how the simulation performed for a twilight orbit gives a scattering angle range that does not cover the rainbow region, thus it never provides with the information needed. Simulations for this orbit are shown in appendix (C). The general results of this simulation is shown in Figure (10.9)

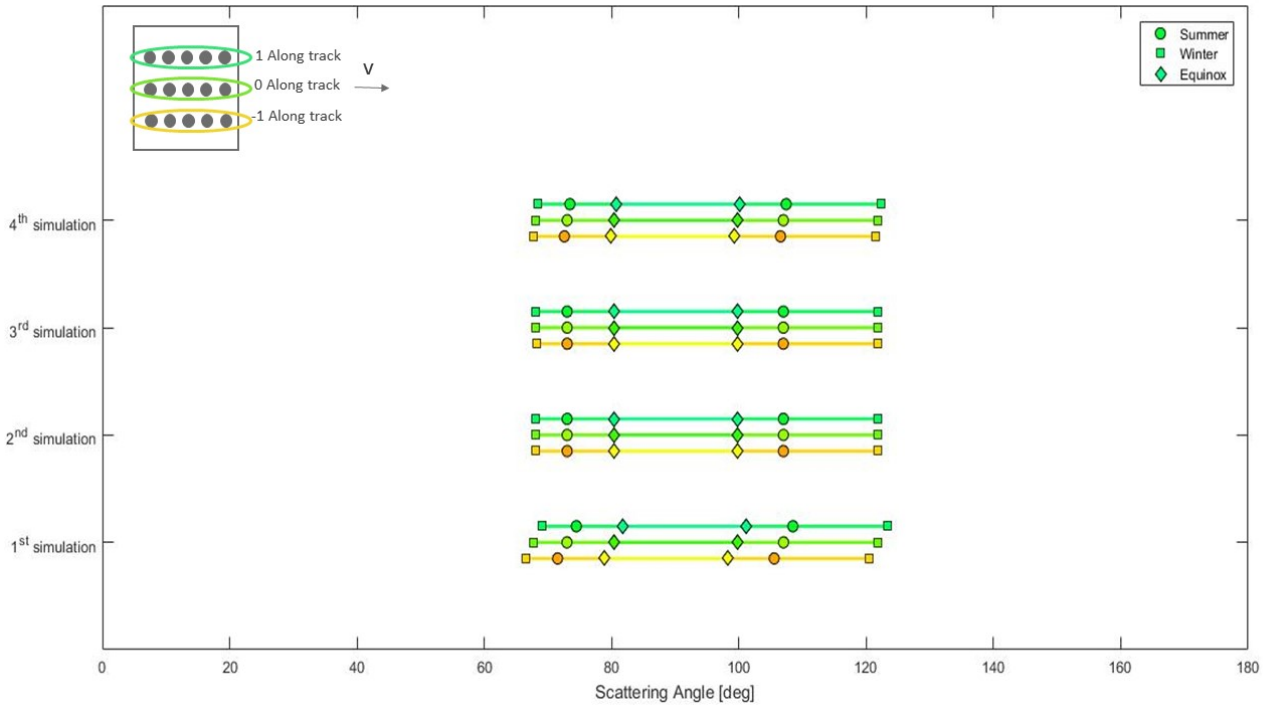

Figure 10.9: Retrieved Scattering angles from the simulations performed using a twilight orbit. It is possible to notice how scattering angles along the orbit never attain the rainbow scattering angle values, around 140^o, thus this orbit loses an important part of the information.

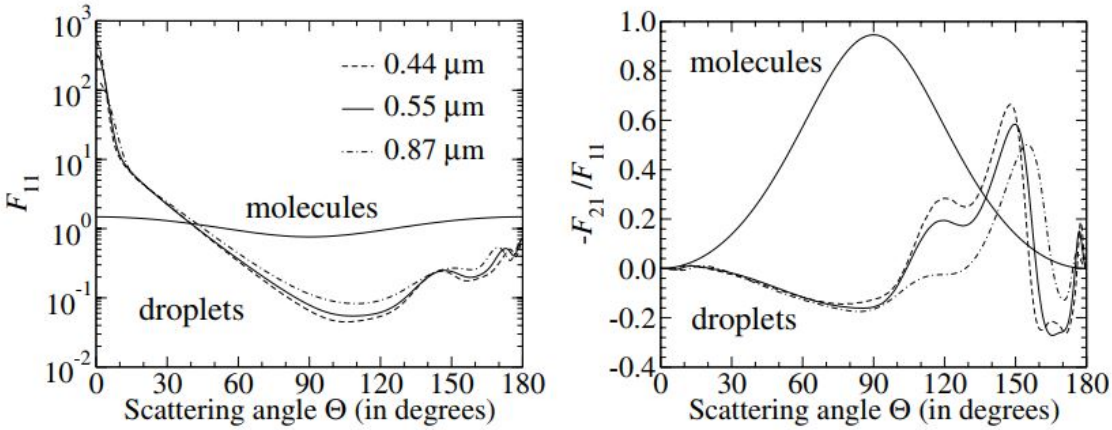

Figure 10.10: Simulation of Intensity and Degree of polarization of observations integrated over the planetary disk, from [2]. In this case the degree of polarization is defined as $-Q/I$ and it has a sign to distinguish polarization on the parallel or perpendicular direction of the scattering plane. The Stokes U is considered zero because the planet is mirror-symmetric with respect to the planetary scattering plane. It is possible to see how the rainbow features is very marked for the degree of polarization and its clear wavelength dependence.

10.2. INTEGRATION

This section will investigate how the final instrument can be built and assembled inside the CubeSat. The research here presented is an initial feasibility study, performed to investigate to what extent it is possible to adapt this technology to this small satellite concept. The

proposed design is just one of the possible applications.

Assuming a SSO type of orbit, results from Section (10.1.2) show that different configurations slightly modify the range of scattering angles retrievable from the satellite. This resulted in the choice of the simplest configuration, the one that guarantees the minimal amount of space and the easiest integration between the fiber head and the spectrograph. For this reason, the second option shown in Figure (10.7) is selected. This configuration corresponds to identical groups of five viewing points oriented along the x axis, that repeat with the same inclination in the cross-track direction (y axis).

This solution is selected mainly because it leads to saving a great amount of space: not having inclined fiber heads in the y direction allows the attachment of the viewing points one to another. The space saved in the y axis allows then to insert another row of viewing points (another group of 5 fiber-heads). This number corresponds to the limit of allowable fibers in the slit (which is also the focal plane) of the spectrograph. The system is then fully exploited in its potentiality.

Other advantages are the decreased complexity of the general payload. Following the CubeSat philosophy of designing something simple, easy to assemble and integrate, this configuration allows the lowest possibility of relative misalignment between different viewing points (since they are parallel to each other in the cross-track direction). It also directly simplifies the design of the connection between fiber-head and spectrograph. As a matter of fact, having identical rows of viewing points allows to replicate the orientation of the fibers for all these groups.

The integration process in the limited space defined by the 1U CubeSat standard started with the placement of the fiber heads, symmetrically disposed in one face of the 3U CubeSat. As a requirement the instrument cannot protrude more than 6.4 mm in the normal direction to the face considered. This configuration is kept inside the 5 mm limit. The spectrograph is then disposed on the opposite side of the 1U cube assumed available for the payload, in order to maximize the space for the fiber connections. The spectrograph is also centered with respect to the viewing side, in order to simplify the design of the fiber connection, since in this way symmetry is maintained.

The biggest peculiarity of optical fibers is that, despite their noticeable flexibility, they show a limited bend radius; if this radius is exceeded a drop in transmission level will be registered. The bend radius value is a fundamental limiting parameter for the integration of the instrument, together with the fibers radii (comprising the cladding thickness) and their numerical apertures.

For the realization of this design, a market research has been performed for the selection of out-of-the-shelf fibers with optimal bend radius properties, with a numerical aperture of 0.22. The selected ones are the Newport model F-MCB-T (Mfg. P/N: CF04406-01) [50] with a long term bend radius of 1.4 cm [1], a fiber diameter of 100 ± 3 μm and a coating diameter of 140 ± 5 μm. With these properties the selected fibers appear to be compatible with the

[1] long term bend radius is the technical specification that indicates the minimum radius tolerated by the fiber over a long period, usually $\sim 16-20$ years.

instrument, a verification can only be performed with a 3D model of the CubeSat. For this purpose the configuration of the viewing point chosen reveals to be particularly suitable, since it presents the extreme case: 20 viewing points, so 40 fibers to be directed in a single spectrograph inside a limited 1U volume (less than the standard $10x10x10\ cm^3$ considering the space subtracted because of the structure).

The results of this integration process are shown in Figure (10.11) that shows a 3D impression of this design with some remarkable measures. Figure (10.12) shows a zoomed representation of the proposed fiber disposition. The fibers are represented as lines, the curvatures are not represented, only the directions and length of the fibers, assuring that they can always allow to realize a bending radius within the maximum tolerated. Appendix D shows the 2D orthogonal projections of the entire instrument and the fiber disposition only.

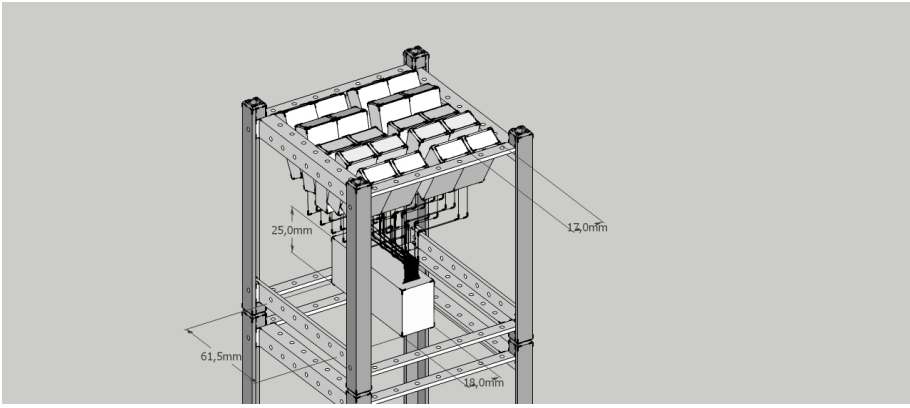

Figure 10.11: 3D representation of the payload on board of the 3U CubeSat. This configuration is built for a "vertical" orientation of the spacecraft. 20 viewing points are used in this configuration arranged as 4 lines in the Along-track direction composed by 5 viewing directions each. The viewing directions comprised in one "line" are inclined ±30 deg, ±15 deg and 0 deg with respect to the normal to the side of the spacecraft where the viewing angles are positioned. These configuration forms then 4 "lines". All of these "lines" are parallel to each other.

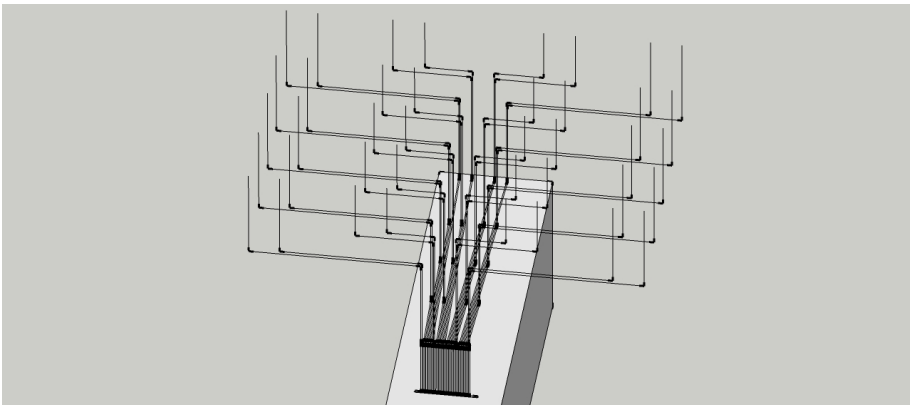

Figure 10.12: Detail on the optical fiber directions and length. This design respects the limit on the bent radius of the optical fibers, which is set to 1.6 cm. The actual curvatures of the fibers are not shown here, but only the directions they have to follow. The 3D representation still shows that it is possible to fit the instrument in the given space. The 40 fibers are all directed at the entrance of one spectrograph.

11

CONCLUSION PART II - DESIGN RESULTS

The second part of the thesis project here reported focused on the feasibility study for the integration of the FlySpex technology inside a small satellite.

The first decision was the choice of the CubeSat 3U platform as a platform to adapt the instrument for. CubeSats are chosen given their global standardization that would drastically ease the design, integration and production effort. Moreover, cost is cut down because of the Off-the-shelf component for the different subsystems and for the launch platforms (P-Pod) that allows to rapidly qualify the CubeSat standard as a secondary payload during any launch campaign.

In the last years the 3U units CubeSat has emerged as the most used standard, adopted by universities for educational purposes and private companies. A market research depicted this CubeSat size as the most used, and in order to retrieve technical requirements for the payload subsystem existing platforms have been considered. These platforms provide assembled spacecraft buses that maximize the payload storing capabilities and they are very versatile in order to adapt to a large variety of missions. According to [34], the 3U platforms are able to host up to a 2.3U payload size with a power supply up to 3.68 W and have a TRL of 9 (data for the GOMX platform developed by GomSpace ApS). In order to include most of the available platforms offered in the market, this feasibility study considered a 1U size for the payload, with a maximum usable power of 1.5 W. This research shown that the FlySpex payload is conform to these stringent requirements.

In order to verify the feasibility of the mission, two approaches were developed, Bottom-Up and Top-Down, that together give an insight on the design of the instrument.

11.1. DIMENSION & POWER BUDGET

From the Bottom-Up approach, dimensions of the spectrograph are studied. The spectrograph uses a grating as a dispersing element and two mirrors to collimate light and increase the system compactness. Results from a first order estimation set the dimensions of the spectrograph to 1.8 x 2.5 x 6.1 cm^3, with a resolution of 4 nm (not considering the aberration introduced by the mirrors and their diffraction limits) and capable of hosting ~ 40 fibers at its entrance slit.

Figure (11.1) shows the simulated effects of this resolution on the retrieved DoLP. For comparison, the real in Lab data are shown, taken with a spectrograph with a resolution of 1.3 nm. This drop in the blue part of the spectra due to the low resolution is corrected during the calibration phase. These effect is shown here in order to show the effect of a drop in the instrument resolution and the procedure to predict it.

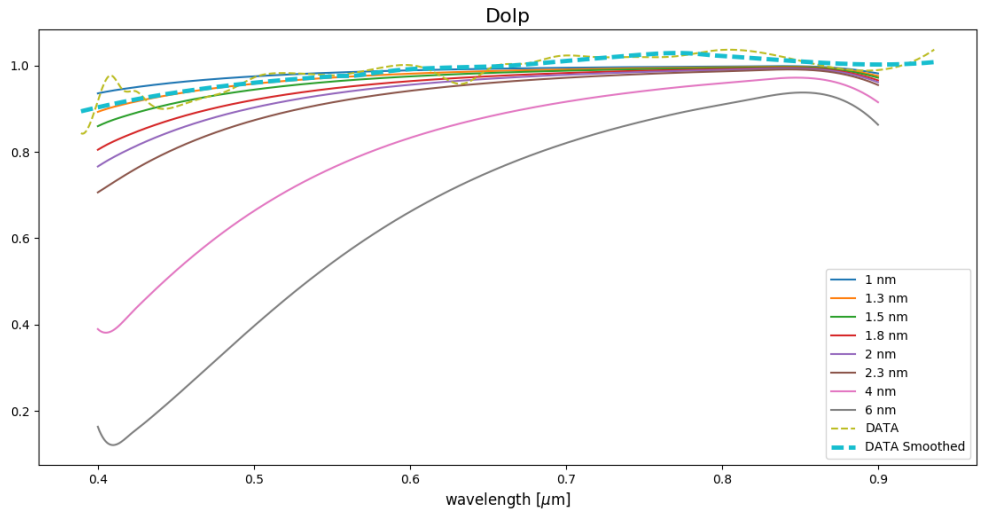

Figure 11.1: Simulated DoLP as they are received at the detector, represented for different resolutions of the spectrograph. Real data from the laboratory test are plotted as dashed line, together with a smoothed version of the line that eliminates the artifacts from the data reduction (a Savitzky-Golay filtering has been applied to the curve). Results are compliant with the expected resolution, since the used spectrograph had a nominal resolution of 1.3 nm.

The discussion on the Detector led to select a model compatible with space and already tested with a similar instrument (SPEX, during the airborne campaign). The detector, a STAR 250 25 μm CMOS, directly defines the power necessities of the instrument, and it has a nominal power specification of 350 mW.

11.2. ACCURACY & VIEWING POINTS

Using a standard Space System Engineering procedure, from the nominal FOV of Fly-SPEX (1^o) the attitude requirement was derived and set to 0.1^o. It has been demonstrated that this requirement is largely satisfied by the available COTS integrated units for attitude active control. These units feature multiple actuators and sensors combined together to increase performances. One of the most promising unit features a pointing capability up to 0.007^o [46], more than an order of magnitude lower error than the required one.

Giving this very high pointing accuracy, the system is assumed not to tumble during operations. For this reason, it is not important to have redundancy on the viewing point directions to account for the spacecraft rotation.

The viewing points configuration is then proposed to be in two directions: along-track and cross-track. Along track directions will help to track the same region under different

viewing angles (thus different scattering angle). Cross-track directions are useful in order to be able to observe a greater area simultaneously and to account for Earth rotation during the orbit. Viewing points oriented along-track are parallel to the velocity direction, and are inclined of $\pm 30^o$, $\pm 15^o$ and 0^o with respect to the normal to the cubeSat surface where the viewing points are oriented. Fibers are all parallel to each other in the cross-track direction, this configuration is chosen because it maximizes the number of available viewing points, optimizing the scientific return of the instrument.

Different configurations are considered and evaluated even though they are harder to design and realize, and do not seem to provide any real improvement on the diversity of scattering angles retrieved, as shown in the simulation performed (Figure (11.1)). For this reason this is considered the preferred option, even though a one-direction configuration can also be evaluated in future iterations if data-rate constraints or weight constraints emerge.

11.3. DATA TRANSMISSION BUDGET

From the conclusion on the number of viewing points a first estimation on the data-rate coming out the detector can be assessed. Considering that the detector's ADC samples at 8 $bit/sample$, each spectra features 400 $nm/4$ $nm = 100$ $samples$: the data produced are thus $D = 800$ bit for every measurement. The $IFOV$ is defined as the width of one pixel, in this case $IFOV = 0.25^o$. Following the estimation proposed in [44], with an orbit velocity of $v_g = 7.588$ Km/s and an along track ground pixels resolution of $Y = IFOV xh = 2.4$ km, the data rate is then $B = \frac{v_g D}{Y} = 2530$ bit/s, or $B = 316.25$ $Bytes/s$ for every spectrum, considering that every viewing point produces 2 spectra and that the viewing points are maximum 20 (as established in the bottom-up analysis), the maximum data rate will then be $B = 101200$ $bits/s = 12,65 Kbytes/s$.

This quantity can either be directly transmitted on the ground or processed. Considering an on-board data processing system, an on-board demodulation of the signal before the down-link is expected, thus three curves are created (Intensity, DoLP and AoLP) and the data rate changes dramatically. If the instrument does not have to retrieve particular features along the spectrum, such gaseous absorption bands, then only few samples are needed to be transmitted. If we suppose to transmit around 20 samples for each of the curves, then the data rate decreases down to $B = 190$ bit/s.

11.4. FUTURE WORK

This work shows the potential and limits of FlySPEX, when applied to a CubeSat standard. The steps to be taken are numerous and they begin with a series of iterations of this feasibility design once a CubeSat platform will be selected and the requirements will evolve in more specific subsystem requirements.

For the Bottom-Up design the next step is about investigating in detail the spectrograph performances. An optimization of the design parameters needs to be performed with a numerical optical tool (e.g. Zemax OpticStudio). This process will define better the complete spectrograph resolution and size that are expected not to diverge much from the value here

presented, that will be used as initial parameters during the optimization process.

The Top-Down approach can be further developed once the other subsystem will be defined with more detail, so that a complete overview of the technological constraints can be used for the design of the instrument. In particular, once the orbit is well defined, a full simulation of the best instrument configurations can be performed again. The work just showed the tool to be used for these simulations, more configurations with different orbit parameters should be experimented.

Appendices

A

TRANSMISSION CORRECTION FORMULA

The complete result of the normalized difference of the two signals (presented on Section 4.2), integrated over a period, is here presented. In order to be more clear, the following parameter will be used:
$a = T_{p1} + T_{s1}$
$b = T_{p1} - T_{s1}$
$c = T_{p2} + T_{s2}$
$d = T_{p2} - T_{s2}$
Substituting these parameters, the results of the integral is:

$$a(\lambda) = \frac{1}{2\pi}\int_0^{2\pi} S(\lambda)\,d\Psi =$$

$$= \frac{b-dt}{b+dt} + \frac{(-4bct+4adt)\,Log\left[(-a+bP_L-ct+dP_Lt)\Big/\sqrt{-a^2-b^2P_L^2-2act+2bdP_L^2t-(d^2P^2-c^2)t^2}\right]}{(b+dt)\sqrt{-a^2-b^2P_L^2-2act+2bdP_L^2t-(d^2P^2-c^2)t^2}} +$$

$$+ \frac{4(bc-ad)\,tLog\left[(a-bP_L+(c-dP_L)t)\Big/\sqrt{-a^2-b^2P_L^2-2act+2bdP_L^2t-(d^2P^2-c^2)t^2}\right]}{(b+dt)\sqrt{-a^2-b^2P_L^2-2act+2bdP_L^2t-(d^2P^2-c^2)t^2}}$$

If we assume $P_L = 1$, similarly to the procedure used in [10], we obtain the following result.

$$a(\lambda) = \frac{1}{2\pi}\int_0^{2\pi} S(\lambda)\,d\Psi \overset{P_L=1}{\approx}$$

$$\approx \frac{b^2+(c-d)dt^2+bct\left(-1+2\sqrt{\frac{a-b+(c-d)t}{a+b+(c+d)t}}\right)+-a\left(b+dt\left(-1+2\sqrt{\frac{a-b+(c-d)t}{a+b+(c+d)t}}\right)\right)}{-(b+dt)[a-b+(c-d)t]}$$

B

TRANSMISSION CORRECTION SIMULATION

Results obtained with an arbitrary chosen transmission ratios varying along the wavelength are shown in Figure (B.1). In order to impose a transmission ratio to the second channel only, a transmission curve was formed from a spline passing through three equidistant points. The transmission curve is shown in Figure (B.2)

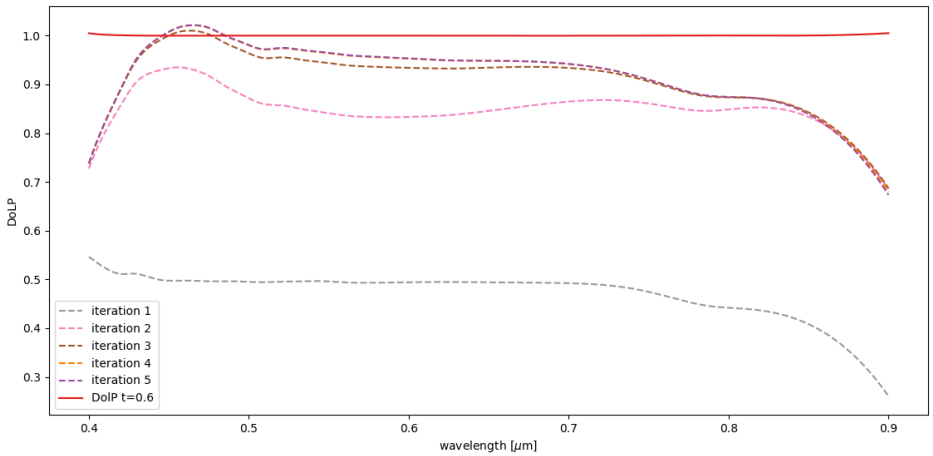

Figure B.1: Application of the correction algorithm to a input curve sat with the use of a non-constant transmission curve. The 4^{th} and 5^{th} iterations (dashd lines) overlap each other, showing algorithm convergence. the red line indicates the result obtained after the extinction ratios correction.

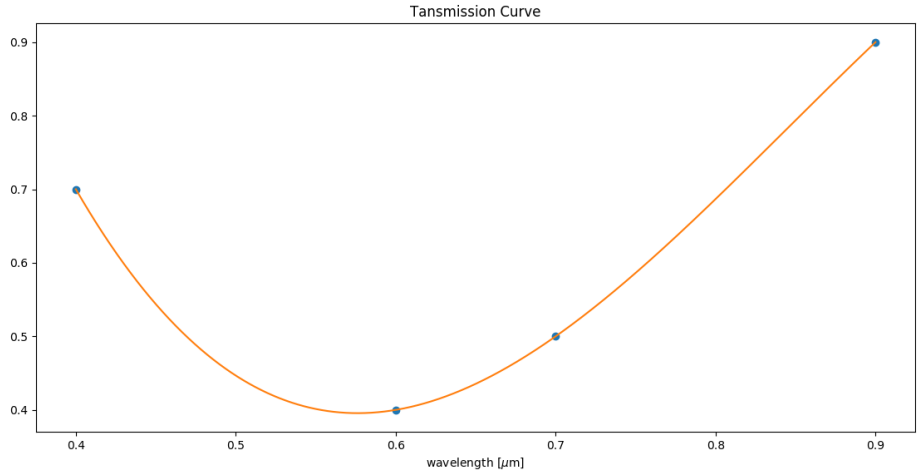

Figure B.2: Transmission curve used for the test of the correction algorithm (extinction ratio and transmission).

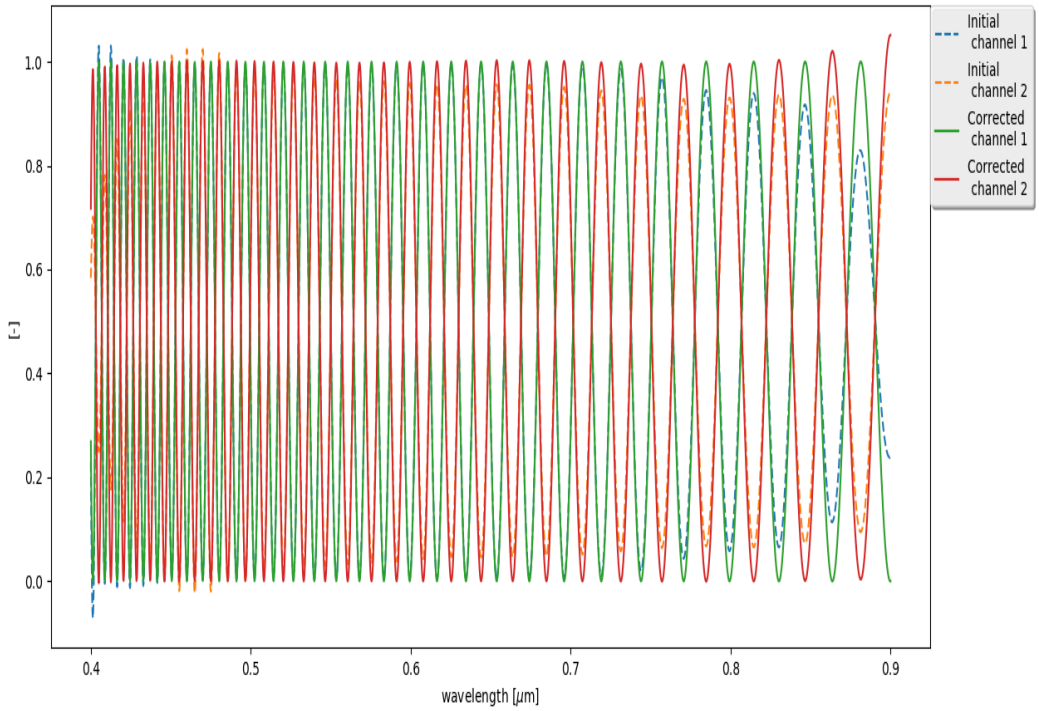

Figure B.3: Correction of the two channels with the transmission and extinction ratios algorithm. Dashed lines show the initial curves, solid lines the final curves obtained from the process.

C

TWILIGHT ORBIT

This appendix shows the results of the scattering angles simulation for a twilight orbit, that passes the ascending nodal point at 6 PM local time. It is noticeable how the retrieved scattering angle range is very limited, since the satellite is always moving along the twilight zone, where the direction of the Sun does not vary much.

It is noticeable how this orbit allows no eclipse for a long period. The spacecraft has no umbra region for simulation during the spring equinox and the summer solstice, suggesting that for a long period (around 6 months), the spacecraft is always illuminated. This is a great advantage for the power supply from the solar panels, but it is here shown that it is not feasible for this type of mission, since the retrieved scattering angles are too limited and they do not cover the rainbow region around 140 deg, as explained before and here demonstrated, in Figure (C.2).

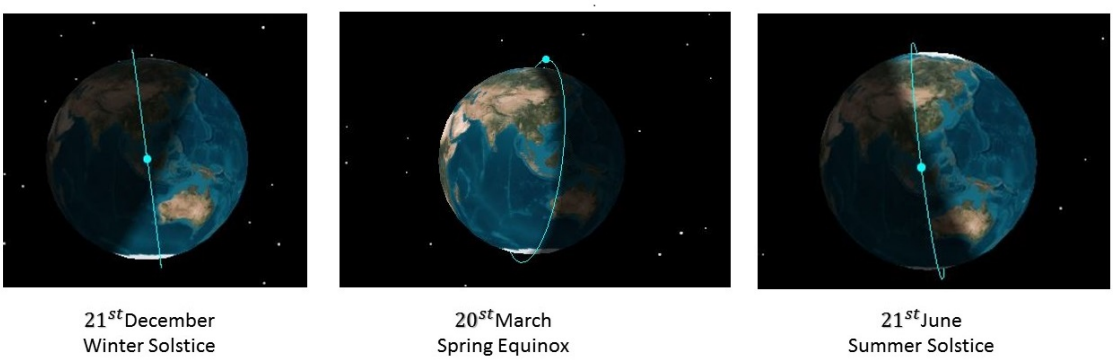

Figure C.1: Representation of a twilight orbit during three different period of the year. The twilight orbit does not enter the Umbra region during the spring equinox and the summer solstice.

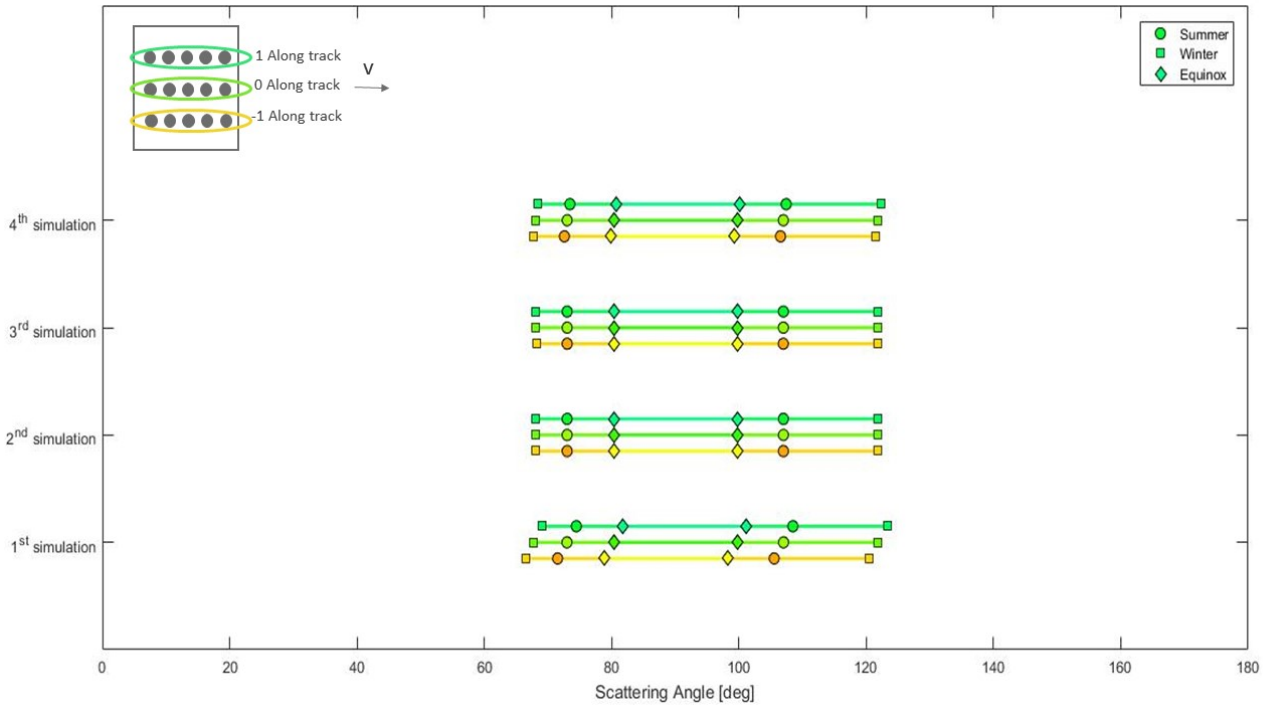

Figure C.2: Retrieved Scattering angles from the simulations performed using a twilight orbit. It is possible to notice how scattering angles along the orbit never attain the rainbow scattering angle values, around 140^o, as previously explained.

D

LAY OUTS

Lay Outs of the chosen configuration for the adaptation of FlySPEX for a Cubesat Standard. A detail on the orientation of the fiber is presented in order to prove that it is possible to connect 40 fibers to the single spectrograph used, in order to have 20 viewing points.

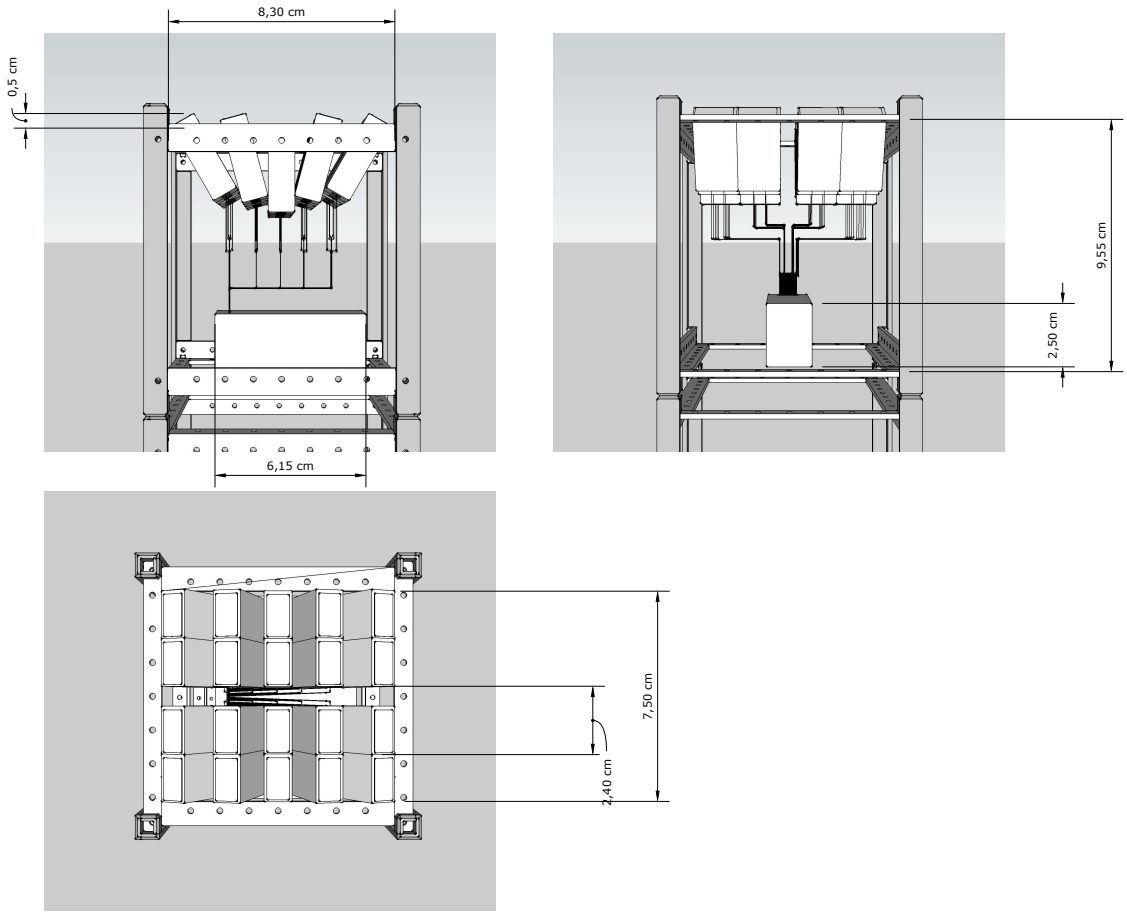

Figure D.1: Orthogonal projections showing the developed concept for the FlySpex instrument. Some measures are presented as a reference. It is noticeable that the fiber head does not exceed the 0.64 cm limitation imposed for surfaces that normally protrude the surface.

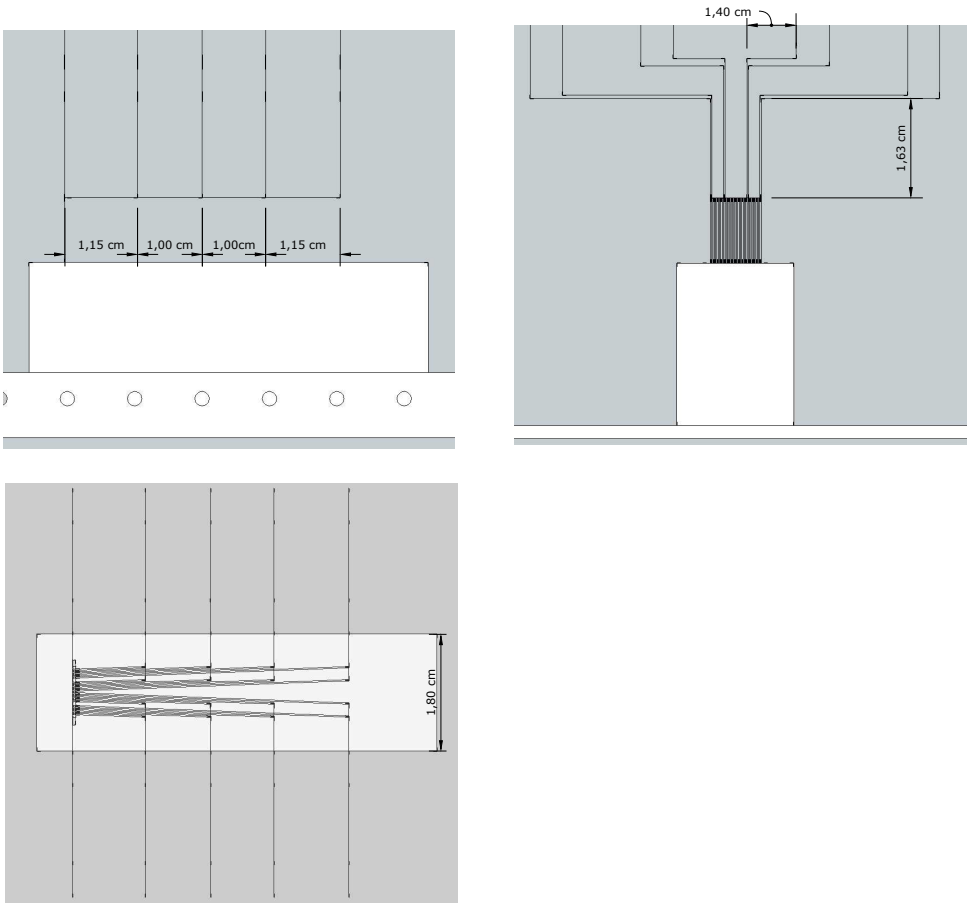

Figure D.2: Detail of the orthogonal projections of the FlySpex instrument focusing on the fibers dispositions.

BIBLIOGRAPHY

[1] H. C Polat, J. Virgili-Llop, and M. Romano, "Survey, statistical analysis and classification of launched cubesat missions with emphasis on the attitude control method," vol. 5, pp. 513–530, 01 2016.

[2] D. Stam, "Spectropolarimetric signatures of earth-like extrasolar planets," *Astronomy & Astrophysics*, vol. 482, no. 3, pp. 989–1007, 2008.

[3] F. Snik, C. U. Keller, M. Wijnen, H. Peters, R. Derks, and E. Smulders, "Flyspex: a flexible multi-angle spectropolarimetric sensing system," in *SPIE Commercial+ Scientific Sensing and Imaging*. International Society for Optics and Photonics, 2016, pp. 985 307–985 307.

[4] T. F. Stocker, D. Qin, G.-K. Plattner, M. Tignor, S. K. Allen, J. Boschung, A. Nauels, Y. Xia, V. Bex, and P. M. e. a. Midgley, "Climate change 2013: The physical science basis," *Intergovernmental Panel on Climate Change, Working Group I Contribution to the IPCC Fifth Assessment Report (AR5)(Cambridge Univ Press, New York)*, 2013.

[5] S. Salvi, "Health effects of ambient air pollution in children," *Paediatric Respiratory Reviews*, vol. 8, no. 4, pp. 275–280, 2007.

[6] C. A. Pope III, R. T. Burnett, M. J. Thun, E. E. Calle, D. Krewski, K. Ito, and G. D. Thurston, "Lung cancer, cardiopulmonary mortality, and long-term exposure to fine particulate air pollution," *Jama*, vol. 287, no. 9, pp. 1132–1141, 2002.

[7] F. Laden, J. Schwartz, F. E. Speizer, and D. W. Dockery, "Reduction in fine particulate air pollution and mortality: extended follow-up of the harvard six cities study," *American journal of respiratory and critical care medicine*, vol. 173, no. 6, pp. 667–672, 2006.

[8] C. A. Pope III and D. W. Dockery, "Health effects of fine particulate air pollution: lines that connect," *Journal of the air & waste management association*, vol. 56, no. 6, pp. 709–742, 2006.

[9] A. Analitis, K. Katsouyanni, K. Dimakopoulou, E. Samoli, A. K. Nikoloulopoulos, Y. Petasakis, G. Touloumi, J. Schwartz, H. R. Anderson, and K. e. a. Cambra, "Short-term effects of ambient particles on cardiovascular and respiratory mortality," *Epidemiology*, vol. 17, no. 2, pp. 230–233, 2006.

[10] G. v. e. a. Harten, *Spectropolarimetry for planetary exploration*. Leiden Observatory, Faculty of Science, Leiden University, 2014.

[11] S. E. Schwartz, "Uncertainty requirements in radiative forcing of climate change," *Journal of the Air & Waste Management Association*, vol. 54, no. 11, pp. 1351–1359, 2004.

[12] O. Hasekamp, "Capability of multi-viewing-angle photo-polarimetric measurements for the simultaneous retrieval of aerosol and cloud properties," *Atmospheric Measurement Techniques*, vol. 3, no. 4, p. 839, 2010.

[13] G. G. Stokes, "On the composition and resolution of streams of polarized light from different sources," *Transactions of the Cambridge Philosophical Society*, vol. 9, p. 399, 1851.

[14] S. Chandrasekhar, *Radiative transfer*. Courier Corporation, 2013, 1946 (first edition).

[15] J. Tinbergen, *Astronomical polarimetry*. Cambridge University Press, 2005.

[16] F. Snik, J. Craven-Jones, M. Escuti, S. Fineschi, D. Harrington, A. De Martino, D. Mawet, J. Riedi, and J. S. Tyo, "An overview of polarimetric sensing techniques and technology with applications to different research fields," in *SPIE Sensing Technology+ Applications*. International Society for Optics and Photonics, 2014, pp. 90 990B–90 990B.

[17] F. Snik and C. U. Keller, "Astronomical polarimetry: Polarized views of stars and planets," in *Planets, Stars and Stellar Systems*. Springer, 2013, pp. 175–221.

[18] J. E. Hansen and L. D. Travis, "Light scattering in planetary atmospheres," *Space science reviews*, vol. 16, no. 4, pp. 527–610, 1974.

[19] J. W. Hovenier, C. V. van der Mee, and H. Domke, *Transfer of polarized light in planetary atmospheres: basic concepts and practical methods*. Springer Science & Business Media, 2014, vol. 318.

[20] E. Collett, "Field guide to polarization," in *SPIE*. SPIE Bellingham, WA, 2005.

[21] D. F. Elmore, *A polarization calibration technique for the advanced stokes polarimeter*. High Altitude Observatory, National Center for Atmospheric Research, 1990.

[22] J. C. del Toro Iniesta and M. Collados, "Optimum modulation and demodulation matrices for solar polarimetry," *Applied Optics*, vol. 39, no. 10, pp. 1637–1642, 2000.

[23] J. S. Tyo, D. L. Goldstein, D. B. Chenault, and J. A. Shaw, "Review of passive imaging polarimetry for remote sensing applications," *Applied optics*, vol. 45, no. 22, pp. 5453–5469, 2006.

[24] M. Semel, J.-F. Donati, and D. Rees, "Zeeman-doppler imaging of active stars. 3: Instrumental and technical considerations," *Astronomy and Astrophysics*, vol. 278, pp. 231–237, 1993.

[25] S. Bagnulo, M. Landolfi, J. Landstreet, E. L. Degl'Innocenti, L. Fossati, and M. Sterzik, "Stellar spectropolarimetry with retarder waveplate and beam splitter devices," *Publications of the Astronomical Society of the Pacific*, vol. 121, no. 883, p. 993, 2009.

[26] K. Oka and T. Kato, "Spectroscopic polarimetry with a channeled spectrum," *Optics Letters*, vol. 24, no. 21, pp. 1475–1477, 1999.

[27] F. J. Iannarilli Jr, S. H. Jones, H. E. Scott, and P. L. Kebabian, "Polarimetric-spectral intensity modulation (p-sim): enabling simultaneous hyperspectral and polarimetric imaging," in *AeroSense'99*. International Society for Optics and Photonics, 1999, pp. 474–481.

[28] K. Nordsieck, "A simple polarimetric system for the lick observatory image-tube scanner," *Publications of the Astronomical Society of the Pacific*, vol. 86, no. 511, p. 324, 1974.

[29] F. Snik, T. Karalidi, and C. U. Keller, "Spectral modulation for full linear polarimetry," *Applied Optics*, vol. 48, no. 7, pp. 1337–1346, 2009.

[30] F. Snik, T. Karalidi, C. Keller, E. Laan, R. ter Horst, R. Navarro, D. Stam, C. Aas, J. de Vries, and G. e. a. Oomen, "Spex: an in-orbit spectropolarimeter for planetary exploration," in *SPIE Astronomical Telescopes+ Instrumentation*. International Society for Optics and Photonics, 2008, pp. 701 015–701 015.

[31] F. Snik, J. H. Rietjens, G. Van Harten, D. M. Stam, C. U. Keller, J. M. Smit, E. C. Laan, A. L. Verlaan, R. Ter Horst, and R. e. a. Navarro, "Spex: the spectropolarimeter for planetary exploration," in *SPIE Astronomical Telescopes+ Instrumentation*. International Society for Optics and Photonics, 2010, pp. 77 311B–77 311B.

[32] A. van Amerongen, J. Rietjens, M. Smit, D. van Loon, and H. e. a. van Brug, "Spex the dutch roadmap towards aerosol measurement from space," in *International Conference on Space Optics*, vol. 18, 2016, p. 21.

[33] A. Poghosyan and A. Golkar, "Cubesat evolution: Analyzing cubesat capabilities for conducting science missions," *Progress in Aerospace Sciences*, vol. 88, pp. 59–83, 2017.

[34] R. Shimmin, E. Agasid, R. Burton, R. Carlino, G. Defouw, A. D. Perez *et al.*, "Small spacecraft technology state of the art," *NASA Ames Research Center, Mission Design Division, NASA/TP-2015-216648/REV1*, 2015.

[35] E. Kulu. nanosats.eu. Accessed on 20-07-2017. [Online]. Available: http://www.nanosats.eu/

[36] P. E. Consortium. Pc/104 specification version 2.6. Accessed on 22-06-2017. [Online]. Available: http://pc104.org/wp-content/uploads/2015/02/PC104_Spec_v2_6.pdf

[37] N. Blind, E. L. Coarer, P. Kern, and S. Gousset, "Spectrographs for astrophotonics," *arXiv preprint arXiv:1707.01669*, 2017.

[38] C. A. Palmer and E. G. Loewen, *Diffraction grating handbook*. Newport Corporation New York, 2005.

[39] S. Grabarnik, R. Wolffenbuttel, A. Emadi, M. Loktev, E. Sokolova, and G. Vdovin, "Planar double-grating microspectrometer," *Optics express*, vol. 15, no. 6, pp. 3581–3588, 2007.

[40] R. F. Wolffenbuttel, "Mems-based optical mini-and microspectrometers for the visible and infrared spectral range," *Journal of Micromechanics and Microengineering*, vol. 15, no. 7, p. S145, 2005.

[41] T. Kawashima, A. Kuze, J. Tanii, S. Mori, T. Ogawa, M. Suzuki, K. Shibasaki, Y. Yamamoto, and T. Sano, "Trade-off studies on odus spectrograph design," in *Proc. SPIE*, vol. 4150, 2001, pp. 400–409.

[42] T. Eversberg and K. Vollmann, *Spectroscopic Instrumentation: Fundamentals and Guidelines for Astronomers*. springer, 2014.

[43] J. C. Lindon, G. E. Tranter, and D. Koppenaal, *Encyclopedia of spectroscopy and spectrometry*. Academic Press, 2016.

[44] J. R. Wertz, D. F. Everett, and J. J. Puschell, *Space mission engineering: the new SMAD*. Microcosm Press, 2011.

[45] D. Selva and D. Krejci, "A survey and assessment of the capabilities of cubesats for earth observation," *Acta Astronautica*, vol. 74, pp. 50–68, 2012.

[46] A. D. Sheet. Blue canyon technologies. Accessed on 22-06-2017. [Online]. Available: http://bluecanyontech.com/wp-content/uploads/2017/07/DataSheet_ADCS_08_F.pdf

[47] G. Krebs. Gunter's space page. Accessed on 20-07-2017. [Online]. Available: http://space.skyrocket.de/

[48] T. Karalidi, D. Stam, and J. Hovenier, "Looking for the rainbow on exoplanets covered by liquid and icy water clouds," *Astronomy & Astrophysics*, vol. 548, p. A90, 2012.

[49] D. Stam, T. Karalidi, and J. Hovenier, "Flux and polarisation spectra of water clouds on exoplanets," *Astronomy & Astrophysics*, vol. 530, p. A69, 2011.

[50] Newport. Fibers f-mcb-t. Accessed on 22-06-2017. [Online]. Available: https://www.newport.com/p/F-MCB-T